

# Limited-angle CT reconstruction via the $L_1/L_2$ minimization\*

Chao Wang<sup>†</sup>, Min Tao<sup>‡</sup>, James Nagy<sup>§</sup>, and Yifei Lou<sup>¶</sup>

**Abstract.** In this paper, we consider minimizing the  $L_1/L_2$  term on the gradient for a limit-angle scanning problem in computed tomography (CT) reconstruction. We design a splitting framework for both constrained and unconstrained optimization models. In addition, we can incorporate a box constraint that is reasonable for imaging applications. Numerical schemes are based on the alternating direction method of multipliers (ADMM), and we provide the convergence analysis of all the proposed algorithms (constrained/unconstrained and with/without the box constraint). Experimental results demonstrate the efficiency of our proposed approaches, showing significant improvements over the state-of-the-art methods in the limit-angle CT reconstruction. Specifically worth noticing is an exact recovery of the Shepp-Logan phantom from noiseless projection data with  $30^\circ$  scanning angle.

**Key words.**  $L_1/L_2$ , sparsity, computed tomography (CT), limited-angle CT

**AMS subject classifications.** 65K10, 68U10, 49N45, 49M20, 92C55

**1. Introduction.** Recent developments in science and technology have led to a revolution in data processing, as large datasets are becoming increasingly available and useful. In medical imaging, a series of imaging modalities, such as x-ray computed tomography (CT) [1, 6, 14, 15], magnetic resonance imaging (MRI) [40], and electroencephalography (EEG) [32, 33], offer different perspectives to facilitate diagnostics. On the other hand, however, one often faces “small data,” e.g., only a small number of CT scans are allowed for the sake of radiation dose. In this paper, we are particularly interested in a limited-angle CT reconstruction problem, which is inevitable in many medical imaging applications. In breast imaging, a technique gaining wide interests is tomosynthesis (sometimes referred to as 3D mammography) [61, 69], which is a limited angle tomography approach designed to produce pseudo three-dimensional images while keeping the radiation exposure to approximately that of traditional two-dimensional mammograms. Other issues to cause limited-angle scanning include short exposure time [29], engine exam [47], and restricted scanning [18].

In order to describe a forward model for the limited-angle problem, we start with a two

---

\*Submitted to the editors May 31, 2020.

**Funding:** M. Tao was supported in part by National Key Research and Development Program of China (2018AAA0101100), and partially by the Jiangsu Provincial Natural Science Foundation of China (No. BK20181257) and partially by the Natural Science Foundation of China (No.11971228). J. Nagy was partially supported by NSF DMS-1819042 and NIH 5R01CA181171-04. Y. Lou was partially supported by NSF grant CAREER 1846690.

<sup>†</sup>Department of Mathematical Sciences, University of Texas at Dallas, Richardson, TX 75080, USA; Department of Radiation Oncology, University of Texas Southwestern Medical Center, Dallas, TX 75390, USA ([chaowang.hk@gmail.com](mailto:chaowang.hk@gmail.com)).

<sup>‡</sup>Department of Mathematics, National Key Laboratory for Novel Software Technology, Nanjing University, Nanjing 210093, China ([taom@nju.edu.cn](mailto:taom@nju.edu.cn)).

<sup>§</sup>Department of Mathematics, Emory University, Atlanta, GA 30322, USA ([jnagy@emory.edu](mailto:jnagy@emory.edu))

<sup>¶</sup>Department of Mathematical Sciences, University of Texas at Dallas, Richardson, TX 75080, USA ([yifei.lou@utdallas.edu](mailto:yifei.lou@utdallas.edu)).

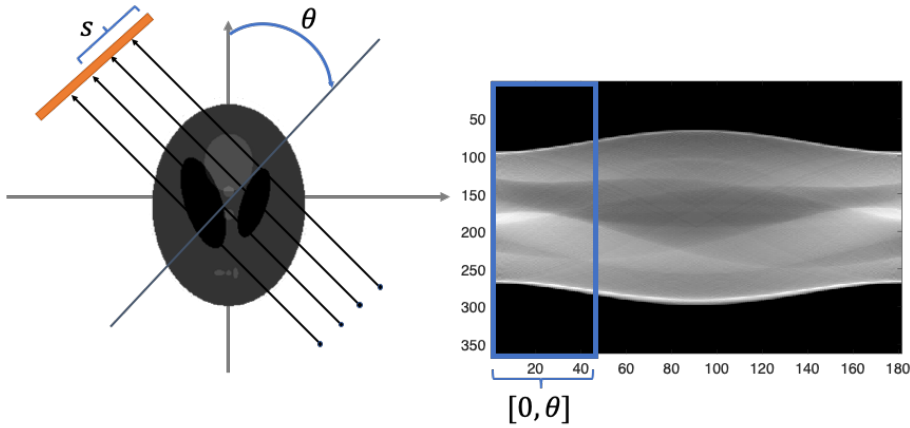


**Figure 1.** Left: illustration on CT projection of parallel beam; Right: limited-angle sinogram (restricted by the blue rectangular).

dimensional parallel-beam CT. The description is analogous to the higher dimension as well as to a fan-beam CT. Mathematically, the projection data  $f$  is obtained by the Radon transform [3] of the attenuation coefficient  $u(x, y) \in L_2(\mathbb{R}^2)$ ,

$$(1.1) \quad f(s, \theta) = \int_{(x,y) \in l(s,\theta)} u(x, y) dx dy = \int_{-\infty}^{+\infty} u(s \cos \theta - r \sin \theta, s \sin \theta + r \cos \theta) dr,$$

where  $\theta$  is the projection angle and  $l(s, \theta)$  represents the line from the x-ray source to the detector element  $s$  at the angle  $\theta$ . The measured data  $f$  at a particular angle is often referred to as *sinogram*. In Figure 1, we illustrate an x-ray projection at an angle of  $\theta = 45^\circ$ , and the corresponding sinogram is one column vector shown on the right plot. A complete (full) scanning is  $\theta$  from  $0^\circ$  to  $180^\circ$ . If we limit the scanning angle to  $[0, \theta]$ , the sinogram restricted by the blue rectangle in Figure 1 is the so-called limited-angle scanning, which is more challenging than the full CT reconstruction.

By stacking  $f, u$  as a vector, we can rewrite the formation model (1.1) into a discretized form  $f = Au$  for a matrix  $A$ . Some conventional methods in the CT reconstruction include filtered back projection (FBP) [16, 53], simultaneous iterative reconstruction technique (SIRT) [3], and simultaneous algebraic reconstruction technique (SART) [2, 28]. These approaches are based on least-squares minimization, i.e., finding  $u$  that minimizes  $\|Au - f\|_2^2$ , but none of them can successfully deal with the limited-angle issue as well as noises in the data, resulting in severe streaking artifacts [17, 44].

When data is insufficient, one often requires reasonable assumptions to be imposed as a regularization term in order to reconstruct a desired solution. One of the most popular regularizations is the total variation (TV) [13, 27, 51, 52, 65], which prefers piece-wise constant images. However, two noticeable drawbacks for TV are loss of contrast and staircasing artifacts. To resolve its limitations, Jia et al. [26] utilized a tight frame regularization and implemented the algorithm on graphics processing units (GPU) to achieve fast computation. Recently, a combination of TV and wavelet tight frame was discussed in [39]. The extension

of TV in a nonlocal fashion by exploiting patch similarity was examined in [38] for the regular CT reconstruction and in [41] for the limited-angle case. Thanks to the recent success of deep learning, machine learning techniques have been introduced to CT reconstruction [4, 58]. Other related applications included sinogram inpainting via a directional TV [54] as well as a joint approach of reconstruction and segmentation [62] for x-ray tomography.

The TV semi-norm is equivalent to the  $L_1$  norm on the gradient. It is well-known that  $L_1$  is the tightest convex approximation to the  $L_0$  norm<sup>1</sup>, which is used to enforce sparsity for signals of interest. There are several alternatives to approximate the  $L_0$  norm, such as  $L_p$  with  $0 < p < 1$  [12, 63], transformed  $L_1$  [42, 55, 67, 68], and  $L_1$ - $L_2$  [34, 35, 36, 43, 64]. Algorithmically, Candés et al. [7] proposed an iteratively reweighted  $L_1$  (IRL1) algorithm to solve for the  $L_0$  minimization. This idea was reformulated as a scale-space algorithm in [25].

Motivated by recent works of using  $L_1/L_2$  [48, 56] for sparse signal recovery, we apply the  $L_1/L_2$  form on the gradient, leading to a new regularization term. This regularization is rather generic in image processing, and we find it works particularly well for piece-wise constant images, owing to its scale-invariant property when approximating  $L_0$ . Extensive experiments demonstrate that our method outperforms the state-of-the-art in CT reconstruction and significant improvements are achieved for the limited-angle case. Although  $L_1/L_2$  on the gradient was originally proposed in [48], it was designed for a constrained problem and lack of convergence analysis. The contributions of this work are three-fold:

1. We propose a new regularization together with a box constraint for CT reconstruction.
2. We design an algorithmic framework for solving several related models.
3. We establish the convergence of all the proposed algorithms.

The rest of the paper is organized as follows. In Section 2, we present some preliminary materials, such as notations, TV definition, and a previous work of  $L_1/L_2$  [48]. We discuss the proposed models and algorithms in Section 3, followed by convergence analysis in Section 4. Experimental studies are conducted in Section 5 using the projection data of two phantoms with and without additive noises. Finally, conclusions and future works are given in Section 6.

**2. Preliminaries.** Suppose an underlying image is defined on an  $m \times n$  Cartesian grid and denote the Euclidean space  $\mathbb{R}^{m \times n}$  as  $X$ . We adopt a linear index for the 2D image, i.e., for  $u \in X$ ,  $u_{ij} \in \mathbb{R}$  is the  $((i-1)m+j)$ -th component of  $u$ . We define a discrete gradient operator,

$$(2.1) \quad \nabla u := (\nabla_x u, \nabla_y u),$$

with  $\nabla_z$  being the forward difference operator in the  $z$ -direction for  $z \in \{x, y\}$ . Denote  $Y = X \times X$ . Then  $\nabla u \in Y$ , and for any  $\mathbf{p} \in Y$ , its  $((i-1)m+j)$ -th component is  $p_{ij} = (p_{ij,1}, p_{ij,2})$ . We use a bold letter  $\mathbf{p}$  to indicate that it contains two elements in each component. With these notations, we define the inner products by

$$(2.2) \quad \langle x, y \rangle_X = \sum_{i,j=1}^{m,n} x_{ij} y_{ij} \quad \text{and} \quad \langle \mathbf{p}, \mathbf{q} \rangle_Y = \sum_{i,j=1}^{m,n} \sum_{k=1}^2 p_{ij,k} q_{ij,k},$$

as well as the corresponding norms

$$(2.3) \quad \|x\|_2 = \sqrt{\langle x, x \rangle_X} \quad \text{and} \quad \|\mathbf{p}\|_2 = \sqrt{\langle \mathbf{p}, \mathbf{p} \rangle_Y}.$$

---

<sup>1</sup>Note that  $L_0$  is not a norm, but often called this way.

**2.1. Total variation.** By incorporating the TV regularization [49] into the data fitting terms, we can obtain the following two models,

$$(2.4) \quad \min_u \|\nabla u\|_1 \quad \text{s.t.} \quad Au = f$$

$$(2.5) \quad \min_u \|\nabla u\|_1 + \frac{\lambda}{2} \|Au - f\|_2^2,$$

where  $\nabla$  is defined in (2.1). We refer (2.4) as a constrained formulation, while (2.5) as an unconstrained one. The latter is often used when the noise is present and the parameter  $\lambda > 0$  in (2.5) shall be tuned according to the noise level. Note that the TV term,  $\|\nabla u\|_1$ , is equivalent to the  $L_1$  norm of the gradient, which can be formulated as the *anisotropic TV*,

$$(2.6) \quad \|\nabla u\|_1 = \|\nabla_x u\|_1 + \|\nabla_y u\|_1,$$

or the *isotropic TV*, defined by  $\sum_{i,j}^{m,n} \sqrt{(\nabla_x u)_{ij}^2 + (\nabla_y u)_{ij}^2}$ . The anisotropic TV was shown to be superior over the isotropic one for CT reconstruction [13]. Here, we also adopt the anisotropic TV to define the  $L_1$  norm on the gradient. Besides, the difference of anisotropic and isotropic TV was proposed in [37] for general imaging applications. There are many efficient algorithms to minimize (2.4) or (2.5), including dual projection [8], primal-dual [9], split Bregman [20], and the alternating direction method of multipliers (ADMM) [5].

**2.2.  $L_1/L_2$  on the gradient.** We review a model of  $L_1/L_2$  on the gradient in a constrained formulation [48],

$$(2.7) \quad \min_u \frac{\|\nabla u\|_1}{\|\nabla u\|_2} \quad \text{s.t.} \quad Au = f,$$

which is referred to as  $L_1/L_2$ -con. Here  $\|\cdot\|_1$  and  $\|\cdot\|_2$  are defined by (2.6) and (2.3), respectively. We apply the ADMM framework [5] to minimize (2.7) by rewriting it into an equivalent form

$$(2.8) \quad \min_{u, \mathbf{d}, \mathbf{h}} \frac{\|\mathbf{d}\|_1}{\|\mathbf{h}\|_2} \quad \text{s.t.} \quad Au = f, \quad \mathbf{d} = \nabla u, \quad \mathbf{h} = \nabla u,$$

with two auxiliary variables  $\mathbf{d}$  and  $\mathbf{h}$ . Note that we denote  $\mathbf{d}$  and  $\mathbf{h}$  in bold to indicate that they have two components corresponding to  $x$  and  $y$  derivatives. The augmented Lagrangian for (2.8) is given by

$$(2.9) \quad \begin{aligned} \mathcal{L}(u, \mathbf{d}, \mathbf{h}; w, \mathbf{b}_1, \mathbf{b}_2) = & \frac{\|\mathbf{d}\|_1}{\|\mathbf{h}\|_2} + \langle \lambda w, f - Au \rangle + \frac{\lambda}{2} \|Au - f\|_2^2 \\ & + \langle \rho_1 \mathbf{b}_1, \nabla u - \mathbf{d} \rangle + \frac{\rho_1}{2} \|\mathbf{d} - \nabla u\|_2^2 \\ & + \langle \rho_2 \mathbf{b}_2, \nabla u - \mathbf{h} \rangle + \frac{\rho_2}{2} \|\mathbf{h} - \nabla u\|_2^2, \end{aligned}$$

where  $w, \mathbf{b}_1, \mathbf{b}_2$  are Lagrange multipliers (or dual variables) and  $\lambda, \rho_1, \rho_2$  are positive parameters. The ADMM iterations proceed as follows,

$$(2.10) \quad \begin{cases} u^{(k+1)} = \arg \min_u \mathcal{L}(u, \mathbf{d}^{(k)}, \mathbf{h}^{(k)}; w^{(k)}, \mathbf{b}_1^{(k)}, \mathbf{b}_2^{(k)}) \\ \mathbf{d}^{(k+1)} = \arg \min_{\mathbf{d}} \mathcal{L}(u^{(k+1)}, \mathbf{d}, \mathbf{h}^{(k)}; w^{(k)}, \mathbf{b}_1^{(k)}, \mathbf{b}_2^{(k)}) \\ \mathbf{h}^{(k+1)} = \arg \min_{\mathbf{h}} \mathcal{L}(u^{(k+1)}, \mathbf{d}^{(k+1)}, \mathbf{h}; w^{(k)}, \mathbf{b}_1^{(k)}, \mathbf{b}_2^{(k)}) \\ w^{(k+1)} = w^{(k)} + f - Au^{(k+1)} \\ \mathbf{b}_1^{(k+1)} = \mathbf{b}_1^{(k)} + \nabla u^{(k+1)} - \mathbf{d}^{(k+1)} \\ \mathbf{b}_2^{(k+1)} = \mathbf{b}_2^{(k)} + \nabla u^{(k+1)} - \mathbf{h}^{(k+1)}. \end{cases}$$

For more details, please refer to [48] that presented a proof-of-concept example when  $A^T A$  and  $\nabla^T \nabla$  can be simultaneously diagonalizable by fast Fourier transform (FFT). Since the splitting scheme (2.8) involves two block variables of  $u$  and  $(\mathbf{d}, \mathbf{h})$ , the existing ADMM convergence results [21, 46, 59] are not applicable. On the other hand, the matrix  $A$  corresponds to a projection matrix in this paper, where the inverse of  $\lambda A^T A + (\rho_1 + \rho_2) \nabla^T \nabla$  can not be efficiently computed via FFT.

**3. The proposed models.** We propose a different splitting scheme, as opposed to (2.8), for solving the constrained problem (2.7); the new scheme has guaranteed convergence. We then extend the same idea to an unconstrained formulation in Section 3.2 and a variant in Section 3.3 to incorporate a box constraint, which is reasonable for imaging applications.

**3.1. Constrained formulation.** The  $L_1/L_2$ -con model (2.7) is equivalent to

$$(3.1) \quad \min_{u, \mathbf{h}} \frac{\|\nabla u\|_1}{\|\mathbf{h}\|_2} + \Pi_{Au=f}(u) \quad \text{s.t.} \quad \mathbf{h} = \nabla u,$$

where  $\Pi_S(t)$  is an indicator function enforcing  $t$  into the feasible set  $S$ , i.e.,

$$(3.2) \quad \Pi_S(t) = \begin{cases} 0 & \text{if } t \in S \\ +\infty & \text{otherwise.} \end{cases}$$

We want to point out that updating  $u, \mathbf{h}$  in (3.1) alternately is different to IRL1 [7], in which the weight is defined elementwise by computing the gradient at every pixel. We adopt ADMM to minimize (3.1) based on the augmented Lagrangian function,

$$(3.3) \quad \mathcal{L}_{\text{con}}(u, \mathbf{h}; \mathbf{b}_2) = \frac{\|\nabla u\|_1}{\|\mathbf{h}\|_2} + \Pi_{Au=f}(u) + \langle \rho_2 \mathbf{b}_2, \nabla u - \mathbf{h} \rangle + \frac{\rho_2}{2} \|\mathbf{h} - \nabla u\|_2^2,$$

where  $\mathbf{b}_2$  is a dual variable and  $\rho_2$  is a positive parameter. Here we use the notation of  $\mathbf{b}_2, \rho_2$  for the consistency to the previous approach (2.10). Then ADMM iterates as follows,

$$(3.4) \quad \begin{cases} u^{(k+1)} = \arg \min_u \mathcal{L}_{\text{con}}(u, \mathbf{h}^{(k)}; \mathbf{b}_2^{(k)}) \\ \mathbf{h}^{(k+1)} = \arg \min_{\mathbf{h}} \mathcal{L}_{\text{con}}(u^{(k+1)}, \mathbf{h}; \mathbf{b}_2^{(k)}) \\ \mathbf{b}_2^{(k+1)} = \mathbf{b}_2^{(k)} + \nabla u^{(k+1)} - \mathbf{h}^{(k+1)}. \end{cases}$$

The update for  $\mathbf{h}$  is the same as in [48], which has a closed-form solution of

$$(3.5) \quad \mathbf{h}^{(k+1)} = \begin{cases} \tau^{(k)} \mathbf{g}^{(k)} & \text{if } \mathbf{g}^{(k)} \neq \mathbf{0} \\ \mathbf{e}^{(k)} & \text{otherwise,} \end{cases}$$

where  $\mathbf{g}^{(k)} = \nabla u^{(k+1)} + \mathbf{b}_2^{(k)}$ ,  $\mathbf{e}^{(k)}$  is a random vector whose  $L_2$  norm is  $\sqrt[3]{\frac{\|\nabla u^{(k+1)}\|_1}{\rho_2}}$ , and  $\tau^{(k)} = \frac{1}{3} + \frac{1}{3}(C^{(k)} + \frac{1}{C^{(k)}})$  with

$$C^{(k)} = \sqrt[3]{\frac{27D^{(k)} + 2 + \sqrt{(27D^{(k)} + 2)^2 - 4}}{2}} \quad \text{and} \quad D^{(k)} = \frac{\|\nabla u^{(k+1)}\|_1}{\rho_2 \|\mathbf{g}^{(k)}\|_2^3}.$$

The  $u$ -subproblem in (3.4) can be expressed as

$$(3.6) \quad u^{(k+1)} = \arg \min_u \frac{\|\nabla u\|_1}{\|\mathbf{h}^{(k)}\|_2} + \frac{\rho_2}{2} \|\mathbf{h}^{(k)} - \nabla u - \mathbf{b}_2^{(k)}\|_2^2 \quad \text{s.t.} \quad Au = f.$$

With  $\mathbf{h}^{(k)}$  and  $\mathbf{b}_2^{(k)}$  fixed, we can apply ADMM to find the optimal solution of (3.6). Specifically by introducing an auxiliary variable  $\mathbf{d}$ , we rewrite (3.6) as

$$(3.7) \quad \min_{u, \mathbf{d}} \frac{\|\mathbf{d}\|_1}{\|\mathbf{h}^{(k)}\|_2} + \frac{\rho_2}{2} \|\mathbf{h}^{(k)} - \nabla u - \mathbf{b}_2^{(k)}\|_2^2 \quad \text{s.t.} \quad Au = f, \quad \mathbf{d} = \nabla u.$$

The augmented Lagrangian corresponding to (3.7) is given by

$$\begin{aligned} \mathcal{L}_{\text{con}}^{(k)}(u, \mathbf{d}; w, \mathbf{b}_1) &= \frac{\|\mathbf{d}\|_1}{\|\mathbf{h}^{(k)}\|_2} + \frac{\rho_2}{2} \|\mathbf{h}^{(k)} - \nabla u - \mathbf{b}_2^{(k)}\|_2^2 \\ &\quad + \langle \lambda w, f - Au \rangle + \frac{\lambda}{2} \|Au - f\|_2^2 + \langle \rho_1 \mathbf{b}_1, \nabla u - \mathbf{d} \rangle + \frac{\rho_1}{2} \|\mathbf{d} - \nabla u\|_2^2, \end{aligned}$$

where  $w, \mathbf{b}_1$  are dual variables and  $\lambda, \rho_1$  are positive parameters. Here we have  $k$  in the superscript of  $\mathcal{L}_{\text{con}}$  to indicate that it is the Lagrangian for the  $u$ -subproblem in (3.4) at the  $k$ -th iteration. The ADMM framework to minimize (3.7) leads to the following iterations,

$$(3.8) \quad \begin{cases} u_{j+1} = \arg \min_u \mathcal{L}_{\text{con}}^{(k)}(u, \mathbf{d}_j; w_j, (\mathbf{b}_1)_j) \\ \mathbf{d}_{j+1} = \arg \min_{\mathbf{d}} \mathcal{L}_{\text{con}}^{(k)}(u_{j+1}, \mathbf{d}; w_j, (\mathbf{b}_1)_j) \\ w_{j+1} = w_j + f - Au_{j+1} \\ (\mathbf{b}_1)_{j+1} = (\mathbf{b}_1)_j + \nabla u_{j+1} - \mathbf{d}_{j+1}, \end{cases}$$

where the subscript  $j$  represents the inner loop index, as opposed to the superscript  $k$  for outer iterations in (3.4). Note that  $\mathcal{L}_{\text{con}}^{(k)}(u, \mathbf{d}; w, \mathbf{b}_1)$  resembles the augmented Lagrangian  $\mathcal{L}(u, \mathbf{d}, \mathbf{h}^{(k)}; w, \mathbf{b}_1, \mathbf{b}_2^{(k)})$  defined in (2.9), and hence (3.4) with one iteration of (3.8) for the  $u$ -subproblem is equivalent to the previous approach [48]. If we can reach to the optimal solution of (3.6), the convergence can be guaranteed; see Section 4.

---

**Algorithm 3.1** The  $L_1/L_2$  constrained minimization ( $L_1/L_2$ -con).

---

```

1: Input: projection matrix  $A$  and observed data  $f$ 
2: Parameters:  $\rho_1, \rho_2, \lambda, \text{kMax}, \text{jMax}$ , and  $\varepsilon \in \mathbb{R}$ 
3: Initialize:  $\mathbf{h}, \mathbf{b}_1, \mathbf{b}_2, \mathbf{d}, w$ , and  $k, j = 0$ 
4: while  $k < \text{kMax}$  or  $|u^{(k)} - u^{(k-1)}|/|u^{(k)}| > \varepsilon$  do
5:   while  $j < \text{jMax}$  or  $|u_j - u_{j-1}|/|u_j| > \varepsilon$  do
6:      $u_{j+1} = (\lambda A^T A - (\rho_1 + \rho_2)\Delta)^{-1}(\lambda A^T(f + w_j) + \rho_1 \nabla^T(\mathbf{d}_j - (\mathbf{b}_1)_j)$ 
        $+ \rho_2 \nabla^T(\mathbf{h}^{(k)} - \mathbf{b}_2^{(k)}))$ 
7:      $\mathbf{d}_{j+1} = \text{shrink}\left(\nabla u_{j+1} + (\mathbf{b}_1)_j, \frac{1}{\rho_1 \|\mathbf{h}^{(k)}\|_2}\right)$ 
8:      $w_{j+1} = w_j + f - Au_{j+1}$ 
9:      $(\mathbf{b}_1)_{j+1} = (\mathbf{b}_1)_j + \nabla u_{j+1} - \mathbf{d}_{j+1}$ 
10:     $j = j + 1$ 
11:   end while
12:   return  $u^{(k+1)} = u_j$ 
13:    $\mathbf{h}^{(k+1)} = \begin{cases} \tau^{(k)}\left(\nabla u^{(k+1)} + \mathbf{b}_2^{(k)}\right) & \nabla u^{(k+1)} + \mathbf{b}_2^{(k)} \neq 0 \\ \mathbf{e}^{(k)} & \text{otherwise} \end{cases}$ 
14:    $\mathbf{b}_2^{(k+1)} = \mathbf{b}_2^{(k)} + \nabla u^{(k+1)} - \mathbf{h}^{(k+1)}$ 
15:    $k = k + 1$  and  $j = 0$ 
16: end while
17: return  $\mathbf{u}^* = \mathbf{u}^{(k)}$ 

```

---

We then elaborate on how to solve the two subproblems in (3.8). By taking derivative of  $\mathcal{L}_{\text{con}}^{(k)}$  with respect to  $u$ , we obtain a closed-form solution given by

$$(3.9) \quad u_{j+1} = \left(\lambda A^T A - (\rho_1 + \rho_2)\Delta\right)^{-1} \left(\lambda A^T(f + w_j) + \rho_1 \nabla^T(\mathbf{d}_j - (\mathbf{b}_1)_j) + \rho_2 \nabla^T(\mathbf{h}^{(k)} - \mathbf{b}_2^{(k)})\right),$$

where  $\Delta = -\nabla^T \nabla$  denotes the Laplacian operator. For a general system matrix  $A$  that can not be diagonalized by Fourier transform, we adopt the conjugate gradient descent iterations [45] to solve for (3.9). The  $\mathbf{d}$ -subproblem in (3.8) also has a closed-form solution, i.e.,

$$(3.10) \quad \mathbf{d}_{j+1} = \text{shrink}\left(\nabla u_{j+1} + (\mathbf{b}_1)_j, \frac{1}{\rho_1 \|\mathbf{h}^{(k)}\|_2}\right),$$

where  $\text{shrink}(\mathbf{v}, \mu) = \text{sign}(\mathbf{v}) \max\{|\mathbf{v}| - \mu, 0\}$ . In summary, we present the overall algorithm to minimize the  $L_1/L_2$ -con model (3.1) in Algorithm 3.1.

**3.2. Unconstrained formulation.** The unconstrained  $L_1/L_2$  problem is given by

$$(3.11) \quad \min_u \frac{\|\nabla u\|_1}{\|\nabla u\|_2} + \frac{\lambda}{2} \|Au - f\|_2^2,$$

which is referred to as  $L_1/L_2$ -uncon. We consider the same splitting scheme as in (3.1) that reformulates (3.11) into

$$(3.12) \quad \min_{u, \mathbf{h}} \frac{\|\nabla u\|_1}{\|\mathbf{h}\|_2} + \frac{\lambda}{2} \|Au - f\|_2^2 \quad \text{s.t.} \quad \mathbf{h} = \nabla u.$$

---

**Algorithm 3.2** The  $L_1/L_2$  unconstrained minimization ( $L_1/L_2$ -uncon).

---

```

1: Input: projection matrix  $A$  and observed data  $f$ 
2: Parameters:  $\rho_1, \rho_2, \lambda, \text{kMax}, \text{jMax}$ , and  $\varepsilon \in \mathbb{R}$ 
3: Initialize:  $\mathbf{h}, \mathbf{b}_1, \mathbf{b}_2, \mathbf{d}$ , and  $k, j = 0$ 
4: while  $k < \text{kMax}$  or  $|u^{(k)} - u^{(k-1)}|/|u^{(k)}| > \varepsilon$  do
5:   while  $j < \text{jMax}$  or  $|u_j - u_{j-1}|/|u_j| > \varepsilon$  do
6:      $u_{j+1} = (\lambda A^T A - (\rho_1 + \rho_2)\Delta)^{-1}(\lambda A^T f + \rho_1 \nabla^T(\mathbf{d}_j - (\mathbf{b}_1)_j)$ 
        $+ \rho_2 \nabla^T(\mathbf{h}^{(k)} - \mathbf{b}_2^{(k)}))$ 
7:      $\mathbf{d}_{j+1} = \text{shrink}\left(\nabla u_{j+1} + (\mathbf{b}_1)_j, \frac{1}{\rho_1 \|\mathbf{h}^{(k)}\|_2}\right)$ 
8:      $(\mathbf{b}_1)_{j+1} = (\mathbf{b}_1)_j + \nabla u_{j+1} - \mathbf{d}_{j+1}$ 
9:      $j = j + 1$ 
10:   end while
11:   return  $u^{(k+1)} = u_j$ 
12:    $\mathbf{h}^{(k+1)} = \begin{cases} \tau^{(k)} \left( \nabla u^{(k+1)} + \mathbf{b}_2^{(k)} \right) & \nabla u^{(k+1)} + \mathbf{b}_2^{(k)} \neq 0 \\ \mathbf{e}^{(k)} & \nabla u^{(k+1)} + \mathbf{b}_2^{(k)} = 0 \end{cases}$ 
13:    $\mathbf{b}_2^{(k+1)} = \mathbf{b}_2^{(k)} + \nabla u^{(k+1)} - \mathbf{h}^{(k+1)}$ 
14:    $k = k + 1$  and  $j = 0$ 
15: end while
16: return  $\mathbf{u}^* = \mathbf{u}^{(k)}$ 

```

---

The corresponding augmented Lagrangian function is expressed as

$$(3.13) \quad \mathcal{L}_{\text{uncon}}(u, \mathbf{h}; \mathbf{b}_2) = \frac{\|\nabla u\|_1}{\|\mathbf{h}\|_2} + \frac{\lambda}{2} \|Au - f\|_2^2 + \langle \rho_2 \mathbf{b}_2, \nabla u - \mathbf{h} \rangle + \frac{\rho_2}{2} \|\mathbf{h} - \nabla u\|_2^2,$$

with a dual variable  $\mathbf{b}_2$  and a positive parameter  $\rho_2$ . The ADMM framework involves the following iterations,

$$(3.14) \quad \begin{cases} \mathbf{u}^{(k+1)} = \arg \min_u \mathcal{L}_{\text{uncon}}(u, \mathbf{h}^{(k)}; \mathbf{b}_2^{(k)}) \\ \mathbf{h}^{(k+1)} = \arg \min_{\mathbf{h}} \mathcal{L}_{\text{uncon}}(u^{(k+1)}, \mathbf{h}; \mathbf{b}_2^{(k)}) \\ \mathbf{b}_2^{(k+1)} = \mathbf{b}_2^{(k)} + \nabla u^{(k+1)} - \mathbf{h}^{(k+1)}. \end{cases}$$

Notice that it has the same structure as (3.4) in the constrained case, especially the same updates for  $\mathbf{h}$  and  $\mathbf{b}_2$ . As a result, we only need to work out the  $u$ -subproblem, which can be expressed equivalently as

$$(3.15) \quad \min_{u, \mathbf{d}} \frac{\|\mathbf{d}\|_1}{\|\mathbf{h}^{(k)}\|_2} + \frac{\lambda}{2} \|Au - f\|_2^2 + \frac{\rho_2}{2} \|\mathbf{h}^{(k)} - \nabla u - \mathbf{b}_2^{(k)}\|_2^2 \quad \text{s.t.} \quad \mathbf{d} = \nabla u.$$

Again we adopt the ADMM scheme to solve for (3.15), which is similar to (3.8). In fact, the only difference is by fixing  $w_j = 0$  for all  $j$ . The details are thus omitted and we summarize in Algorithm 3.2 for minimizing the  $L_1/L_2$ -uncon (3.11).



**3.3. Box constraint.** It is reasonable to incorporate a box constraint for image processing applications [10, 30], since pixel values are usually bounded by  $[0, 1]$  or  $[0, 255]$ . Specifically for CT, the pixel value has physical meanings and hence the bound can often be estimated in advance [1, 6]. The box constraint is particularly helpful for the  $L_1/L_2$  model to prevent its divergence [56]. We can add a box constraint  $u \in [c, d]$  to both constrained (2.7) and unconstrained (3.11) formulations, thus leading to

$$(3.16) \quad \min_u \frac{\|\nabla u\|_1}{\|\nabla u\|_2} \quad \text{s.t.} \quad Au = f, u \in [c, d]$$

$$(3.17) \quad \min_u \frac{\|\nabla u\|_1}{\|\nabla u\|_2} + \frac{\lambda}{2} \|Au - f\|_2^2 \quad \text{s.t.} \quad u \in [c, d],$$

referred to as  $L_1/L_2$ -con-box and  $L_1/L_2$ -uncon-box, respectively. Here we derive an algorithm for solving the  $L_1/L_2$ -con-box model; the unconstrained version follows similarly. We can rewrite (3.16) equivalently as

$$(3.18) \quad \min_{u, \mathbf{h}} \frac{\|\nabla u\|_1}{\|\mathbf{h}\|_2} + \Pi_{Au=f}(u) + \Pi_{[c,d]}(u) \quad \text{s.t.} \quad \mathbf{h} = \nabla u,$$

where  $\Pi_S(t)$  is the indicator function defined in (3.2). By using ADMM, we have the same update rules for  $\mathbf{h}$  and  $\mathbf{b}_2$  as in (3.4), while the  $u$ -subproblem is given by

$$(3.19) \quad u^{(k+1)} = \arg \min_u \frac{\|\nabla u\|_1}{\|\mathbf{h}^{(k)}\|_2} + \frac{\rho_2}{2} \|\mathbf{h}^{(k)} - \nabla u - \mathbf{b}_2^{(k)}\|_2^2 \quad \text{s.t.} \quad Au = f, u \in [c, d].$$

We introduce two variables,  $\mathbf{d}$  for the gradient and  $v$  for the box constraint, thus getting

$$(3.20) \quad \min_{u, \mathbf{d}, v} \frac{\|\mathbf{d}\|_1}{\|\mathbf{h}^{(k)}\|_2} + \frac{\rho_2}{2} \|\mathbf{h}^{(k)} - \nabla u - \mathbf{b}_2^{(k)}\|_2^2 + \Pi_{[c,d]}(v) \quad \text{s.t.} \quad Au = f, \mathbf{d} = \nabla u, u = v.$$

The augmented Lagrangian corresponding to (3.20) becomes

$$(3.21) \quad \begin{aligned} \mathcal{L}_{\text{box}}^{(k)}(u, \mathbf{d}, v; w, \mathbf{b}_1, e) &= \frac{\|\mathbf{d}\|_1}{\|\mathbf{h}^{(k)}\|_2} + \frac{\rho_2}{2} \|\nabla u - \mathbf{h}^{(k)} + \mathbf{b}_2^{(k)}\|_2^2 + \Pi_{[c,d]}(v) \\ &\quad + \langle \lambda w, f - Au \rangle + \frac{\lambda}{2} \|Au - f\|_2^2 \\ &\quad + \langle \rho_1 \mathbf{b}_1, \nabla u - \mathbf{d} \rangle + \frac{\rho_1}{2} \|\mathbf{d} - \nabla u\|_2^2 \\ &\quad + \langle \beta e, u - v \rangle + \frac{\beta}{2} \|v - u\|_2^2, \end{aligned}$$

where  $w, \mathbf{b}_1, e$  are dual variables and  $\lambda, \rho_1, \beta$ , are positive parameters. Similar to (3.8), there is a closed-form solution of the  $u$ -subproblem,

$$(3.22) \quad \begin{aligned} u_{j+1} &= \left( \lambda A^T A - (\rho_1 + \rho_2) \Delta \right)^{-1} \left( \lambda A^T (f + w_j) \right. \\ &\quad \left. + \rho_1 \nabla^T (\mathbf{d}_j - (\mathbf{b}_1)_j) + \rho_2 \nabla^T (\mathbf{h}^{(k)} - \mathbf{b}_2^{(k)}) + \beta (v^{(k)} - e^{(k)}) \right). \end{aligned}$$

The update for  $\mathbf{d}$  is the same as (3.10), and we update  $v$  by projecting it onto  $[c, d]$ , i.e.,  $v_{j+1} = \min \{ \max \{ u_{j+1} + e_j, c \}, d \}$ . Similarly, we can get an algorithm for minimizing the  $L_1/L_2$ -uncon-box model by fixing  $w_j = 0$  for all  $j$ . The pseudo-code for both constrained and unconstrained versions is summarized in [Algorithm 3.3](#).

---

**Algorithm 3.3** The  $L_1/L_2$  minimization with a box constraint ( $L_1/L_2$ -box).

---

1: Input: projection matrix  $A$ , observed data  $f$ , and a bound  $[c, d]$  for the original image  
2: Parameters:  $\rho_1, \rho_2, \lambda, \beta, \text{kMax}, \text{jMax}$ , and  $\epsilon \in \mathbb{R}$   
3: Initialize:  $\mathbf{h}, \mathbf{b}_1, \mathbf{b}_2, \mathbf{d}, w = 0, e$ , and  $k, j = 0$   
4: **while**  $k < \text{kMax}$  or  $|u^{(k)} - u^{(k-1)}|/|u^{(k)}| > \epsilon$  **do**  
5:   **while**  $j < \text{jMax}$  or  $|u_j - u_{j-1}|/|u_j| > \epsilon$  **do**  
6:      $u_{j+1} = (\lambda A^T A - (\rho_1 + \rho_2)\Delta)^{-1}(\lambda A^T(f + w_j) + \rho_1 \nabla^T(\mathbf{d}_j - (\mathbf{b}_1)_j)$   
       $+ \rho_2 \nabla^T(\mathbf{h}^{(k)} - \mathbf{b}_2^{(k)}) + \beta(v^{(k)} - e^{(k)}))$   
7:      $\mathbf{d}_{j+1} = \text{shrink}\left(\nabla u_{j+1} + (\mathbf{b}_1)_j, \frac{1}{\rho_1 \|\mathbf{h}^{(k)}\|_2}\right)$   
8:      $v_{j+1} = \min\{\max\{u_{j+1} + e_j, c\}, d\}$   
9:      $w_{j+1} = w_j + f - Au_{j+1}$    only for the  $L_1/L_2$ -con-box  
10:      $(\mathbf{b}_1)_{j+1} = (\mathbf{b}_1)_j + \nabla u_{j+1} - \mathbf{d}_{j+1}$   
11:      $e_{j+1} = e_j + u_{j+1} - v_{j+1}$   
12:      $j = j + 1$   
13:   **end while**  
14:   **return**  $u^{(k+1)} = u_j$   
15:    $\mathbf{h}^{(k+1)} = \begin{cases} \tau^{(k)}\left(\nabla u^{(k+1)} + \mathbf{b}_2^{(k)}\right) & \nabla u^{(k+1)} + \mathbf{b}_2^{(k)} \neq 0 \\ \mathbf{e}^{(k)} & \nabla u^{(k+1)} + \mathbf{b}_2^{(k)} = 0 \end{cases}$   
16:    $\mathbf{b}_2^{(k+1)} = \mathbf{b}_2^{(k)} + \nabla u^{(k+1)} - \mathbf{h}^{(k+1)}$   
17:    $k = k + 1$  and  $j = 0$   
18: **end while**  
19: **return**  $\mathbf{u}^* = \mathbf{u}^{(k)}$

---

**4. Convergence analysis.** We intend to establish the convergence of all the algorithms (Algorithm 3.1-Algorithm 3.3) discussed in the previous section. We observe that the ADMM framework for all these models share the same structure

$$(4.1) \quad \begin{cases} u^{(k+1)} = \arg \min_u \mathcal{L}(u, \mathbf{h}^{(k)}; \mathbf{b}_2^{(k)}) \\ \mathbf{h}^{(k+1)} = \arg \min_{\mathbf{h}} \mathcal{L}(u^{(k+1)}, \mathbf{h}; \mathbf{b}_2^{(k)}) \\ \mathbf{b}_2^{(k+1)} = \mathbf{b}_2^{(k)} + \nabla u^{(k+1)} - \mathbf{h}^{(k+1)}, \end{cases}$$

where  $\mathcal{L}$  is either  $\mathcal{L}_{\text{con}}$ ,  $\mathcal{L}_{\text{uncon}}$ , or  $\mathcal{L}_{\text{box}}$ . We show that for  $\mathcal{L}_{\text{con}}$  and  $\mathcal{L}_{\text{uncon}}$ , the sequence generated by ADMM either diverges due to unboundedness or has a convergent subsequence, while the sequence for  $\mathcal{L}_{\text{box}}$  always has a convergent subsequence. For this purpose, we introduce Lemma 4.2 for an upper bound of  $\|\mathbf{b}_2^{(k+1)} - \mathbf{b}_2^{(k)}\|_2$  in terms of  $\|u^{(k+1)} - u^{(k)}\|_2$  and  $\|\mathbf{h}^{(k+1)} - \mathbf{h}^{(k)}\|_2$ . Lemma 4.3 and Lemma 4.4 are standard in convergence analysis [24, 31, 57, 59] to guarantee that the augmented Lagrangian decreases sufficiently and the subgradient at each iteration is bounded by successive errors, respectively. The lemmas require the following three assumptions,

- A1 :  $\mathcal{N}(\nabla) \cap \mathcal{N}(A) = \{0\}$ , where  $\mathcal{N}$  denotes the null space and  $\nabla$  is defined in (2.1).
- A2 : The sequence  $\{u^{(k)}\}$  generated by (4.1) is bounded, then so is  $\{\nabla u^{(k)}\}$  and we denote  $M = \sup_k \{\|\nabla u^{(k)}\|_1\}$ .

A3 : The norm of  $\{\mathbf{h}^{(k)}\}$  generated by (4.1) has a lower bound, i.e., there exist a positive constant  $\epsilon$  such that  $\|\mathbf{h}^{(k)}\|_2 \geq \epsilon, \forall k$ .

*Remark 4.1.* The assumption A1 is standard in image processing [11, 37]. The assumption A2 requires the boundedness of  $\{u^{(k)}\}$ , and hence the convergence results can be interpreted as the sequence either diverges (due to unboundedness) or converges to a critical point. To make the  $L_1/L_2$  regularization well-defined, we shall have  $\|\mathbf{h}\|_2 > 0$ . Certainly,  $\|\mathbf{h}\|_2 > 0$  does not imply a uniform lower bound of  $\epsilon$ , but we can redefine the divergence of an algorithm by including the case of  $\|\mathbf{h}^{(k)}\|_2 < \epsilon$ , which can be checked numerically with a pre-set value of  $\epsilon$ .

Please refer to Appendix for the proofs of these lemmas, based on which we can establish the convergence in Theorem 4.5-Theorem 4.7 for Algorithm 3.1-Algorithm 3.3, respectively.

**Lemma 4.2.** *Under the assumptions A1 and A2, the sequence  $\{u^{(k)}, \mathbf{h}^{(k)}, \mathbf{b}_2^{(k)}\}$  generated by (4.1) satisfies*

$$(4.2) \quad \left\| \mathbf{b}_2^{(k+1)} - \mathbf{b}_2^{(k)} \right\|_2^2 \leq \left( \frac{32mn}{\rho_2^2 \epsilon^4} \right) \left\| u^{(k+1)} - u^{(k)} \right\|_2^2 + \left( \frac{32M^2}{\rho_2^2 \epsilon^6} \right) \left\| \mathbf{h}^{(k+1)} - \mathbf{h}^{(k)} \right\|_2^2.$$

**Lemma 4.3.** *(sufficient descent) Under the assumptions A1-A3 and a sufficiently large  $\rho_2$ , the sequence  $\{u^{(k)}, \mathbf{h}^{(k)}, \mathbf{b}_2^{(k)}\}$  generated by (4.1) satisfies*

$$(4.3) \quad \mathcal{L}(u^{(k+1)}, \mathbf{h}^{(k+1)}; \mathbf{b}_2^{(k+1)}) \leq \mathcal{L}(u^{(k)}, \mathbf{h}^{(k)}; \mathbf{b}_2^{(k)}) - c_1 \|u^{(k+1)} - u^{(k)}\|_2^2 - c_2 \|\mathbf{h}^{(k+1)} - \mathbf{h}^{(k)}\|_2^2,$$

where  $c_1$  and  $c_2$  are two positive constants.

**Lemma 4.4.** *(subgradient bound) Under the assumptions A1-A3 and a sufficiently large  $\rho_2$ , there exists a vector  $\boldsymbol{\eta}^{(k+1)} \in \partial \mathcal{L}(u^{(k+1)}, \mathbf{h}^{(k+1)}; \mathbf{b}_2^{(k+1)})$  and a constant  $\gamma > 0$  such that*

$$(4.4) \quad \|\boldsymbol{\eta}^{(k+1)}\|_2^2 \leq \gamma \left( \|\mathbf{h}^{(k+1)} - \mathbf{h}^{(k)}\|_2^2 + \|\mathbf{b}_2^{(k+1)} - \mathbf{b}_2^{(k)}\|_2^2 \right).$$

**Theorem 4.5.** *(convergence of  $L_1/L_2$ -con) Under the assumptions A1-A3 and a sufficiently large  $\rho_2$ , the sequence  $\{u^{(k)}, \mathbf{h}^{(k)}\}$  generated by (3.4) has a subsequence convergent to a critical point of (3.1).*

*Proof.* We first show that if  $\{u^{(k)}\}$  is bounded, then  $\{\mathbf{h}^{(k)}, \mathbf{b}_2^{(k)}\}$  is also bounded. As  $\|u^{(k)}\|_2$  is bounded, so is  $\|\nabla u^{(k)}\|_1$ . It follows from the assumption A2 and the optimality condition for  $\mathbf{b}_2$  in (A.3) that we have

$$\|\mathbf{b}_2^{(k)}\|_2 = \left\| \frac{\|\nabla u^{(k)}\|_1}{\rho_2} \frac{\mathbf{h}^{(k)}}{\|\mathbf{h}^{(k)}\|_2^3} \right\|_2 \leq \frac{\|\nabla u^{(k)}\|_1}{\rho_2 \epsilon^2}.$$

Therefore,  $\{\mathbf{b}_2^{(k)}\}$  is bounded and hence  $\{\mathbf{h}^{(k)}\}$  is also bounded due to the  $\mathbf{h}$ -update (3.5) and boundedness of  $\nabla u$ . Then it follows from the Bolzano-Weierstrass Theorem that the sequence  $\{u^{(k)}, \mathbf{h}^{(k)}, \mathbf{b}_2^{(k)}\}$  has a convergent subsequence, denoted by  $(u^{(k_j)}, \mathbf{h}^{(k_j)}, \mathbf{b}_2^{(k_j)}) \rightarrow (u^*, \mathbf{h}^*, \mathbf{b}_2^*)$ ,

as  $k_j \rightarrow \infty$ . In addition, we can estimate that

$$\begin{aligned} & \mathcal{L}_{\text{con}}(u^{(k)}, \mathbf{h}^{(k)}; \mathbf{b}_2^{(k)}) \\ &= \frac{\|\nabla u^{(k)}\|_1}{\|\mathbf{h}^{(k)}\|_2} + \Pi_{Au=f}(u^{(k)}) + \frac{\rho_2}{2} \|\mathbf{h}^{(k)} - \nabla u^{(k)} - \mathbf{b}_2\|_2^2 - \frac{\rho_2}{2} \|\mathbf{b}_2^{(k)}\|_2^2 \\ &\geq \frac{\|\nabla u^{(k)}\|_1}{\|\mathbf{h}^{(k)}\|_2} - \frac{\|\nabla u^{(k)}\|_1^2}{\rho_2 \epsilon^4}, \end{aligned}$$

which gives a lower bound of  $\mathcal{L}_{\text{con}}$  owing to the boundedness of  $u^{(k)}$  and  $\mathbf{h}^{(k)}$ . Therefore,  $\mathcal{L}_{\text{con}}(u^{(k)}, \mathbf{h}^{(k)}, \mathbf{b}_2^{(k)})$  converges due to its monotonic decreasing by [Lemma 4.3](#).

We then sum the inequality [\(4.3\)](#) from  $k = 0$  to  $K$ , thus getting

$$\begin{aligned} & \mathcal{L}_{\text{con}}(u^{(K+1)}, \mathbf{h}^{(K+1)}; \mathbf{b}_2^{(K+1)}) \\ &\leq \mathcal{L}_{\text{con}}(u^{(0)}, \mathbf{h}^{(0)}; \mathbf{b}_2^{(0)}) - c_1 \sum_{k=0}^K \|u^{(k+1)} - u^{(k)}\|_2^2 - c_2 \sum_{k=0}^K \|\mathbf{h}^{(k+1)} - \mathbf{h}^{(k)}\|_2^2. \end{aligned}$$

Let  $K \rightarrow \infty$ , we have both summations of  $\sum_{k=0}^{\infty} \|u^{(k+1)} - u^{(k)}\|_2^2$  and  $\sum_{k=0}^{\infty} \|\mathbf{h}^{(k+1)} - \mathbf{h}^{(k)}\|_2^2$  are finite, indicating that  $u^{(k)} - u^{(k+1)} \rightarrow 0$ ,  $\mathbf{h}^{(k)} - \mathbf{h}^{(k+1)} \rightarrow 0$ . Then by [Lemma 4.2](#), we get  $\mathbf{b}_2^{(k)} - \mathbf{b}_2^{(k+1)} \rightarrow 0$ . By  $(u^{(k_j)}, \mathbf{h}^{(k_j)}, \mathbf{b}_2^{(k_j)}) \rightarrow (u^*, \mathbf{h}^*, \mathbf{b}_2^*)$ , we have  $(u^{(k_j+1)}, \mathbf{h}^{(k_j+1)}, \mathbf{b}_2^{(k_j+1)}) \rightarrow (u^*, \mathbf{h}^*, \mathbf{b}_2^*)$ ,  $Au^* = f$  (as  $Au^{(k_j)} = f$ ), and  $\nabla u^* = \mathbf{h}^*$  (by the update of  $\mathbf{b}_2$ ). By [Lemma 4.4](#), we have  $\mathbf{0} \in \mathcal{L}_{\text{con}}(u^*, \mathbf{h}^*, \mathbf{b}_2^*)$  and hence  $(u^*, \mathbf{h}^*)$  is a critical point of [\(3.1\)](#).  $\blacksquare$

**Theorem 4.6.** (convergence of  $L_1/L_2$ -uncon) Under the assumptions [A1-A3](#) and a sufficiently large  $\rho_2$ , the sequence  $\{u^{(k)}, \mathbf{h}^{(k)}\}$  generated by [\(3.14\)](#) has a subsequence convergent to a critical point of [\(3.12\)](#).

The proof is similar to [Theorem 4.5](#), thus omitted. For the box-constrained models [\(3.16\)](#)-[\(3.17\)](#) with an explicit bounded assumption on  $u$ , we can prove that the ADMM framework has the same convergence results as in [Theorem 4.5](#) and [Theorem 4.6](#) without the assumption [A2](#). The proof is omitted as well.

**Theorem 4.7.** (convergence of  $L_1/L_2$ -box) Under the assumptions [A1](#), [A3](#), and a sufficiently large  $\rho_2$ , the sequence  $\{u^{(k)}, \mathbf{h}^{(k)}\}$  generated by [Algorithm 3.3](#) always has a subsequence convergent to a critical point of either [\(3.16\)](#) for  $L_1/L_2$ -con-box or [\(3.17\)](#) for  $L_1/L_2$ -uncon-box.

**5. Experimental results.** In this section, we carry out extensive experiments to demonstrate the performance of the proposed approaches. All the numerical experiments are conducted on a desktop with CPU (Intel i7-5930K, 3.50 GHz) and MATLAB 9.7 (R2019b). For testing, we use two standard phantoms: Shepp-Logan (SL) [\[50\]](#) and FORBILD (FB) [\[66\]](#), shown in [Figure 2](#). Notice that the FB phantom has a very low image contrast and we display it with the grayscale window of  $[1.03, 1.10]$  in order to reveal its structures. For simplicity, we scale the pixel value to  $[0, 1]$  for both phantoms and rescale the solution back after the computation. To synthesize the limited-angle CT projected data, we discretize both phantoms at a resolution of  $256 \times 256$ . The forward operator  $A$  is generated as the discrete Radon



**Figure 2.** Ground truth of Shepp-Logan (SL) phantom and FORBILD (FB) head phantom with the gray scale window of  $[0, 1]$  and  $[1.03, 1.10]$ , respectively.

transform with a parallel beam geometry sampled at  $\theta_{\text{Max}}/30$  over a range of  $\theta_{\text{Max}}$ , resulting in a sub-sampled data of size  $362 \times 31$ . Note that we use the same number of projections when we vary ranges of projection angles. The simulation process is available in the IR and AIR toolbox [19, 22].

We evaluate the performance in terms of the relative error (RE), the overall structural similarity index (SSIM) [60], and the peak signal-to-noise ratio (PSNR) [60]. RE is defined as

$$\text{RE}(u^*, \tilde{u}) := \frac{\|u^* - \tilde{u}\|_2}{\|\tilde{u}\|_2},$$

where  $u^*$  is the restored image and  $\tilde{u}$  is the ground truth. SSIM is the mean of local similarity indices,

$$\text{SSIM}(u^*, \tilde{u}) := \frac{1}{N} \sum_{i=1}^N \text{ssim}(x_i, y_i),$$

where  $x_i, y_i$  are corresponding the  $i$ -th  $8 \times 8$  windows for  $u^*$  and  $\tilde{u}$ , respectively, and  $N$  is the number of such windows. The local similarity index is defined as

$$\text{ssim}(x, y) := \frac{(2\mu_x\mu_y + c_1)(2\sigma_{xy} + c_2)}{(\mu_x^2 + \mu_y^2 + c_1)(\sigma_x^2 + \sigma_y^2 + c_2)},$$

where the averages/variances of  $x, y$  are denoted as  $\mu_x/\sigma_x^2$  and  $\mu_y/\sigma_y^2$ , respectively. Here,  $c_1$  and  $c_2$  are two fixed constants to stabilize the division with weak denominator, which are set to be  $c_1 = c_2 = 0.05$ . Lastly, PSNR is defined as

$$(5.1) \quad \text{PSNR}(u^*, \tilde{u}) := 10 \log_{10} \frac{mnR^2}{\|u^* - \tilde{u}\|_2^2},$$

where  $R$  is the maximum peak value of the original image  $\tilde{u} \in \mathbb{R}^{m \times n}$ .

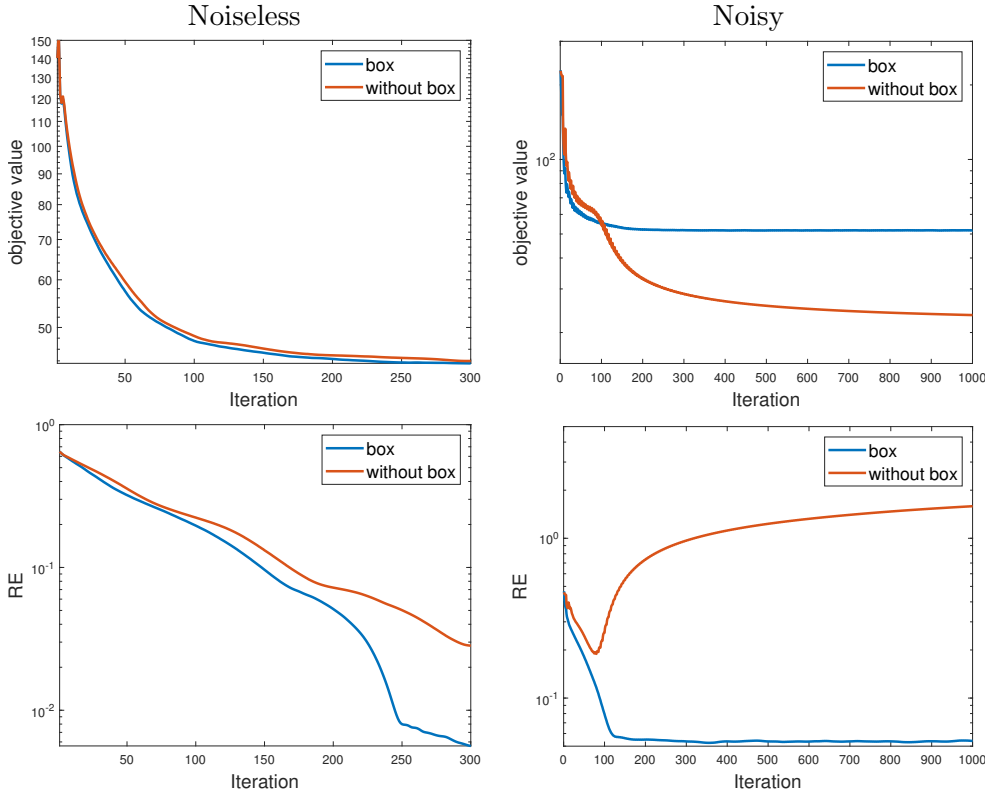


**Figure 3.** The effects of the box constraint in terms of the objective value (top) and the relative error (bottom) in the noiseless (left) and noisy (right) cases.

**5.1. Algorithm behavior.** We first discuss two computational aspects of the proposed algorithms. In particular, we want to analyze the influence of the box constraint as well as the maximum number of inner iterations (denoted by  $\text{jMax}$ ) on the reconstruction results. We consider the SL phantom with the scanning range of  $45^\circ$  for the noiseless case and  $135^\circ$  with a noise level of 0.5%. The fidelity of the CT reconstruction and the convergence are assessed in terms of objective values and  $\text{RE}(u^{(k)}, \tilde{u})$  versus outer iteration counter  $k$ .

In **Figure 3**, we present algorithmic behaviors of the box constraint on both constrained and unconstrained models. Note that the objective function of the constrained model in the noiseless case is  $\frac{\|\nabla u\|_1}{\|\nabla u\|_2}$ , while it is  $\frac{\|\nabla u\|_1}{\|\nabla u\|_2} + \frac{\lambda}{2}\|Au - f\|_2^2$  for the unconstrained case. Here we set  $\text{jMax}$  to be 1 and 5 for noiseless and noisy cases, respectively (we will discuss the effects of inner iteration number shortly.) We plot both inner and outer iterations in **Figure 3**, showing that the proposed algorithms (with and without the box constraint) are convergent, as the objective functions decrease. On the other hand, the box constraint yields smaller relative errors in both cases compared to without box. Specifically in the noisy case, the box constraint helps to avoid local minimizers, as the relative error of the algorithm without constraints increases and the objective function keeps going down. For the rest of the experiments, we only consider the algorithms with a  $[0, 1]$  box constraint.

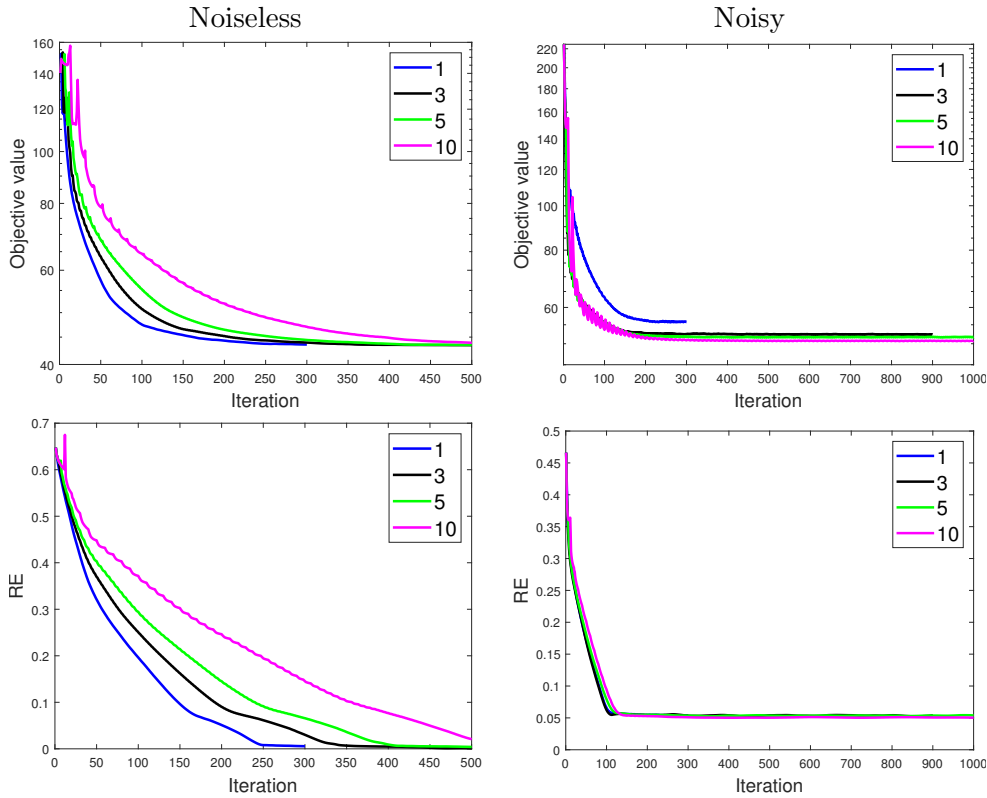


**Figure 4.** The effects of the maximum number in the inner loops with respect to the objective value (top) and the relative error (bottom) in the noiseless (left) and noisy (right) cases.

We then discuss the influence of  $jMax$  on the sparse recovery performance. Fixing the maximum outer iterations as 300, we examine the results of  $jMax=1, 3, 5,$  and  $10$  for both noiseless and noisy cases. In Figure 4, we plot the objective values and relative errors with respect to iterations (counting both inner and outer loops). In the noiseless case, we observe that one inner iteration is sufficient to yield satisfactory results in terms of both objective value and RE. In the noisy case, the objective function with only one inner iteration does not decrease as much as the ones with more inner iterations. Following Figure 4, we set  $jMax$  to be 1 and 5 in the noiseless and noisy cases, respectively, for the rest of the experiments.

**5.2. Noiseless case.** In the noiseless case, we compare the constrained  $L_1/L_2$  model (2.7) with a clinical standard approach of SART [2] and the TV model (2.4), referred to as  $L_1$ . For both  $L_1/L_2$  and  $L_1$  models, we present results with the  $[0, 1]$  box constraint. For fair comparison, we set the initial condition of  $u$  to be a zero vector for all the methods. The (outer) stopping criterion is  $\frac{\|u^{(k)} - u^{(k-1)}\|_2}{\|u^{(k)}\|_2} \leq 10^{-5}$ . Following the discussion in Subsection 5.1, we set  $jMax=1$  for the subproblem. In Table 1, we record RE, SSIM, and PSNR to evaluate CT reconstruction results under different scan ranges for the two phantoms. As the SL phantom is relatively simpler than FB, we test under an extremely limited angle of only  $30^\circ$  scanning range. For all the results presented in Table 1,  $L_1/L_2$  achieves perfect SSIM scores

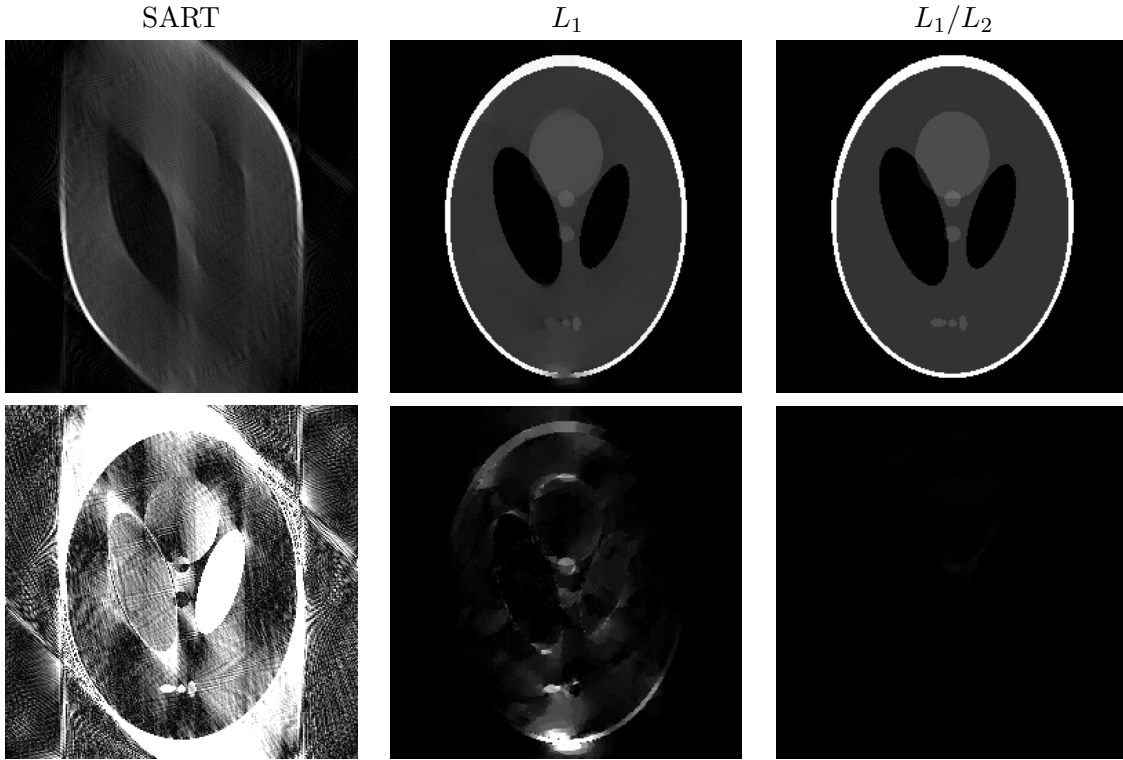


**Figure 5.** Noiseless case: CT reconstruction from  $45^\circ$  projection range for the SL phantom. The top row is the restored images with gray scale window  $[0, 1]$  and the bottom row is the absolute difference between the restored image and ground truth with gray scale window  $[0, 0.1]$ .  $L_1/L_2$  yields the perfect recovery.

and significant improvements over SART and  $L_1$  in terms of RE and PSNR.

Visually, we present the CT reconstruction results of  $45^\circ$  projection range for SL (SL- $45^\circ$ ) and  $75^\circ$  for FB (FB- $75^\circ$ ) in [Figure 5](#) and [Figure 6](#), respectively. In the first case (SL- $45^\circ$ ), SART fails to recover the ellipse inside of the skull with such a small range of projection angles. Both  $L_1$  and  $L_1/L_2$  perform much better owing to their sparsity promoting property. However, the  $L_1$  model is unable to restore the bottom skull and preserve details of some ellipses in the middle. The proposed  $L_1/L_2$  method leads an almost exact recovery with a relative error of 0.64% and visually no difference to the ground truth. In the second case (FB- $75^\circ$ ), none of the methods can get an exact recovery, although  $L_1/L_2$  can achieve the perfect SSIM score of 1. When we show the images with the window of  $[1.0, 1.2]$ , we observe some fluctuations inside of the skull. Among the competing methods,  $L_1/L_2$  restores the most details of the image. We plot the horizontal and vertical profiles in [Figure 7](#), which illustrates that  $L_1/L_2$  leads to the smallest fluctuations compared to the other methods. We also observe a well-known artifact of the  $L_1$  method, i.e., loss of contrast, as its profile fails to reach the height of jump on the intervals such as  $[160, 180]$  in the left plot and  $[220, 230]$  in the right plot of [Figure 7](#), while  $L_1/L_2$  has a good recovery in these regions.



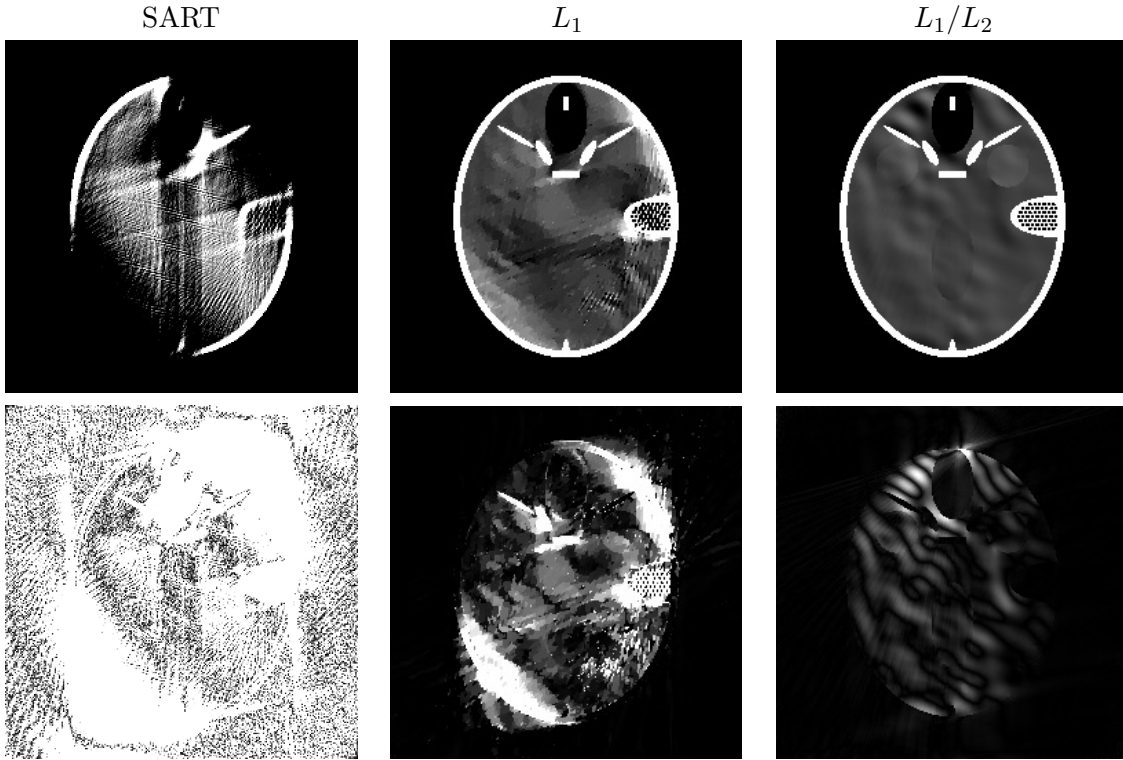


**Figure 6.** Noiseless case: CT reconstruction from  $75^\circ$  projection range for the FB phantom. The top row is the restored images with gray scale window  $[1.0, 1.2]$  and the bottom row is the absolute difference between the restored image and ground truth with the gray scale window  $[0, 0.05]$ .

**Table 1**

Noiseless case: CT reconstruction by SART,  $L_1$ , and  $L_1/L_2$ .

phantom	range	SART			$L_1$			$L_1/L_2$		
		SSIM	PSNR	RE	SSIM	PSNR	RE	SSIM	PSNR	RE
SL	$30^\circ$	0.59	15.66	66.95%	0.98	28.33	15.60%	1.00	56.11	0.64%
	$45^\circ$	0.61	16.08	63.78%	0.99	33.33	8.75%	1.00	70.18	0.13%
	$60^\circ$	0.59	15.66	66.95%	1.00	43.37	2.75%	1.00	68.83	0.15%
FB	$60^\circ$	0.39	15.61	40.16%	0.96	25.43	13.00%	1.00	46.97	1.09%
	$75^\circ$	0.48	16.14	37.79%	0.99	28.84	8.76%	1.00	49.30	0.83%
	$90^\circ$	0.50	16.64	35.68%	1.00	69.68	0.08%	1.00	70.57	0.07%

**5.3. Noisy case.** We add Gaussian noise with different noise levels (1%, 0.5%, and 0.1%) to the projected data for both phantoms. The standard deviation of the simulated noise is the noise level multiplied by the maximum intensity of the projected image. In the noisy case, we set the maximum iteration in the inner loop and outer loop of the  $L_1/L_2$  method as 5 and 300, respectively, while the maximum iteration of  $L_1$  is 500. Similar to the noiseless case, we incorporate the  $[0, 1]$  box constraint in both  $L_1$  and  $L_1/L_2$  models.

We present the CT reconstruction results under various noise levels in [Tables 2](#) and [3](#) for SL and FB phantoms, respectively. Starting the projection range from  $90^\circ$  to  $180^\circ$  each with

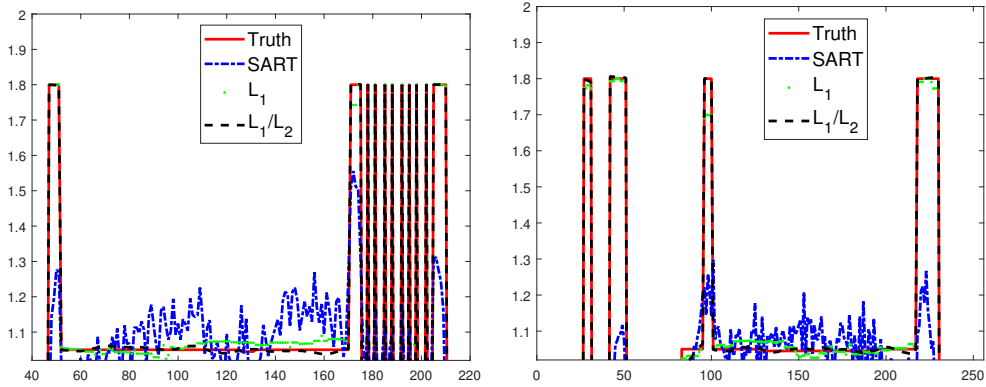


**Figure 7.** Noiseless case: horizontal and vertical profiles generated via SART,  $L_1$ , and  $L_1/L_2$  in the range of projection  $75^\circ$  for the FB phantom.

the same number of projections, all the methods yield better performance when there is less noise with a larger range of scanning angle. Overall, the proposed  $L_1/L_2$  approach achieves significant improvements over SART and  $L_1$ .

**Table 2**

Noisy case: CT reconstruction of the SL phantom by SART,  $L_1$ , and  $L_1/L_2$ .

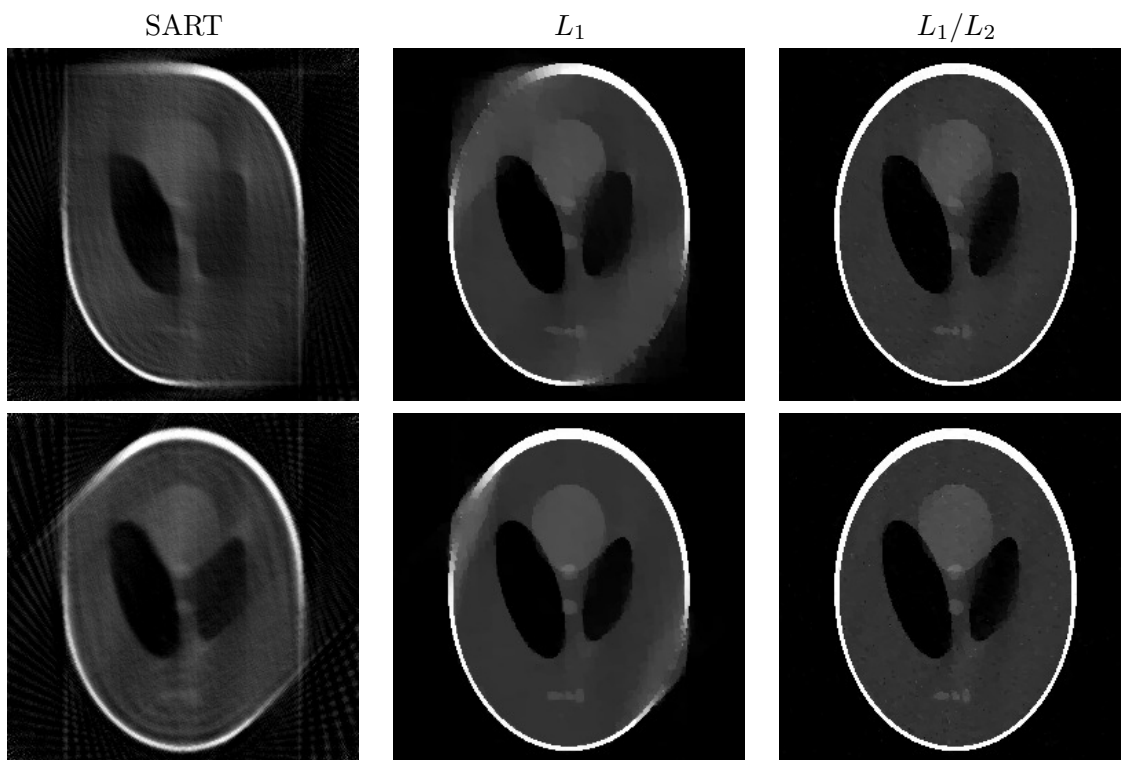
noise	range	SART			$L_1$			$L_1/L_2$		
		SSIM	PSNR	RE	SSIM	PSNR	RE	SSIM	PSNR	RE
1%	$90^\circ$	0.51	16.92	57.86%	0.87	19.97	40.74%	0.84	25.14	22.48%
	$135^\circ$	0.53	18.40	48.83%	0.92	23.30	27.77%	0.86	28.12	15.94%
	$180^\circ$	0.53	19.69	42.06%	0.98	34.56	7.59%	0.99	40.13	4.00%
0.5%	$90^\circ$	0.57	18.87	46.27%	0.89	20.21	39.62%	0.97	35.68	6.68%
	$135^\circ$	0.57	18.87	46.27%	0.95	23.93	25.84%	0.97	37.17	5.62%
	$180^\circ$	0.57	20.21	39.64%	0.99	39.54	4.28%	1.00	44.52	2.41%
0.1%	$90^\circ$	0.58	17.28	55.57%	0.97	28.36	15.52%	1.00	52.83	0.93%
	$135^\circ$	0.60	19.01	45.49%	0.96	24.25	24.89%	1.00	58.91	0.46%
	$180^\circ$	0.58	20.40	38.77%	1.00	45.86	2.07%	1.00	60.54	0.38%

In [Figure 8](#), we show the CT reconstruction of the SL phantom in the cases of  $90^\circ$  and  $135^\circ$  projection range, both with 0.5% noise level. Our proposed method is able to preserve more structures than SART and  $L_1$ , both of which fail to recover two sides of the skull. On the other hand, the  $L_1$  approach is better at the flat surface, where the proposed  $L_1/L_2$  model produces some oscillatory patterns. In [Figure 9](#), we have similar observations for the FB phantom in 0.1% noise. Although the proposed approach yields salt-and-pepper type of artifacts, it gives better results compared to the other competing methods. We present the profile plots in [Figure 10](#), which shows that our approach performs very well, especially for the boundary and high contrast details.

**6. Conclusions and future works.** Following a preliminary work [\[48\]](#), we considered the use of  $L_1/L_2$  on the gradient as a regularization for imaging applications. We formulated both constrained and unconstrained models, the latter of which is novel and suitable when the noise

**Table 3***Noisy case: CT reconstruction of the FB phantom by SART,  $L_1$ , and  $L_1/L_2$ .*

noise	range	SART			$L_1$			$L_1/L_2$		
		SSIM	PSNR	RE	SSIM	PSNR	RE	SSIM	PSNR	RE
1%	90°	0.36	15.57	40.35%	0.80	20.43	23.07%	0.91	22.05	19.13%
	135°	0.38	17.01	34.19%	0.84	23.09	16.98%	0.95	25.10	13.47%
	180°	0.40	17.93	30.75%	0.87	25.70	12.57%	0.96	27.68	10.01%
0.5%	90°	0.44	16.36	36.85%	0.91	22.25	18.70%	0.89	27.36	10.39%
	135°	0.47	18.18	29.86%	0.95	25.36	13.08%	0.91	30.16	7.52%
	180°	0.47	19.59	25.40%	0.98	30.71	7.06%	1.00	36.27	3.72%
0.1%	90°	0.50	16.62	35.74%	0.94	23.96	15.37%	0.99	41.11	2.13%
	135°	0.52	18.67	28.25%	0.97	26.75	11.14%	1.00	54.85	0.44%
	180°	0.52	20.19	23.70%	1.00	35.61	4.02%	1.00	55.61	0.40%

**Figure 8.** *Noisy case: CT reconstruction from 90° (top) and 135° (bottom) projection range for the SL phantom with 0.5% noise. The gray scale window [0, 1].*

is present. We also incorporated a box constraint that is reasonable and yet helpful for the CT reconstruction problem. We provided convergence guarantees for all the algorithms under mild conditions. We conducted extensive experiments to demonstrate that our approaches outperform the state-of-the-art in the limited-angle CT reconstruction with and without additive noises. Specifically, the proposed approach yields an exact recovery of the Shepp-Logan phantom from noiseless projection data with only 30° scanning angle.

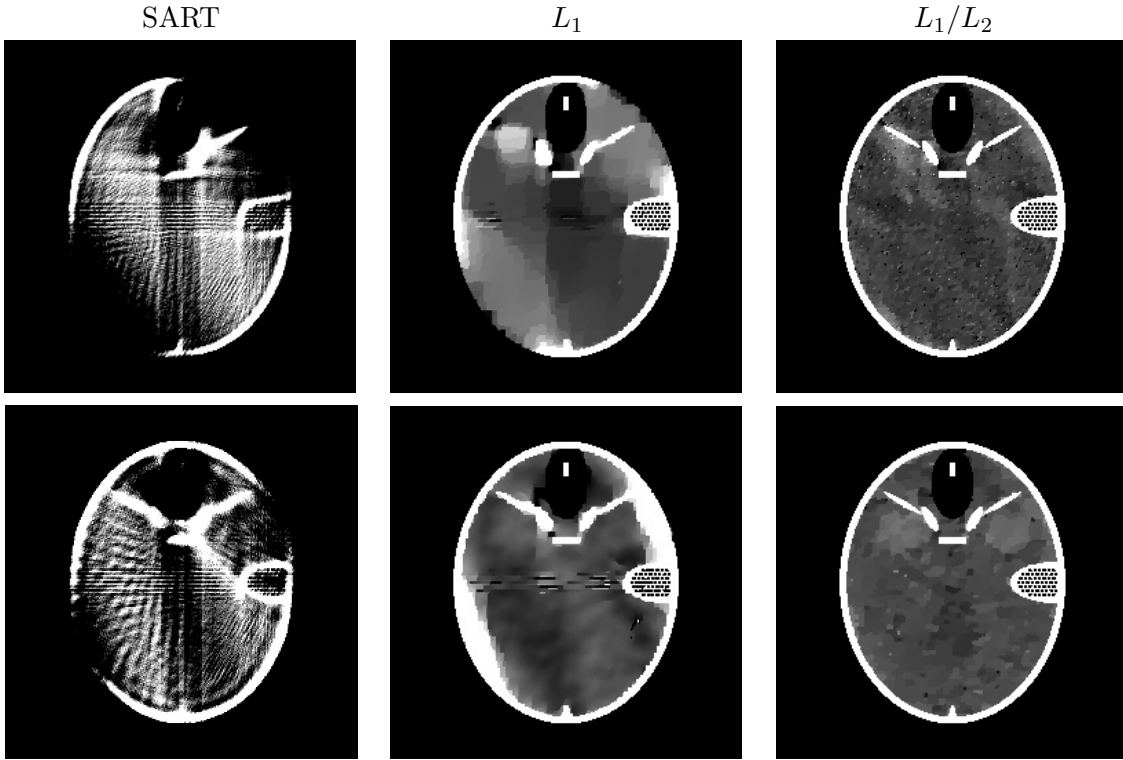


**Figure 9.** Noisy case: CT reconstruction from  $90^\circ$  (top) and  $135^\circ$  (bottom) projection range for the FB phantom with 0.1% noise. The gray scale window is  $[0, 0.05]$ .

In reality, Poisson distribution is more appropriate than Gaussian distribution to describe the noise statistics of the projection data. Consequently, one future direction involves using different data fitting terms, as opposed to the least squares, for the CT reconstruction with noise. As both  $L_1$  and  $L_1/L_2$  models take about 10 minutes to run on MATLAB, we plan to implement the algorithms on the GPU for fast computation. Besides, the extensions to a higher dimension as well as to other medical and biological applications with real data, e.g., MRI, cone-beam CT, positron emission tomography (PET), and transmission electron microscopy (TEM), are worth exploring in the future.

**Appendix A. Proofs.** To prepare for convergence analysis, we summarize some equivalent conditions for strong convexity and Lipschitz smooth functions in [Lemma A.1](#) and [Lemma A.2](#), respectively.

**Lemma A.1.** A function  $f(x)$  is called strongly convex with parameter  $\mu$  if and only if one of the following conditions holds

- (a)  $g(x) = f(x) - \frac{\mu}{2}\|x\|_2^2$  is convex;
- (b)  $\langle \nabla f(x) - \nabla f(y), x - y \rangle \geq \mu\|x - y\|_2^2, \forall x, y$ ;
- (c)  $f(y) \geq f(x) + \langle \nabla f(x), y - x \rangle + \frac{\mu}{2}\|y - x\|_2^2, \forall x, y$ .

**Lemma A.2.** The gradient of  $f(x)$  is Lipschitz continuous with parameter  $L > 0$  if and only if one of the following conditions holds

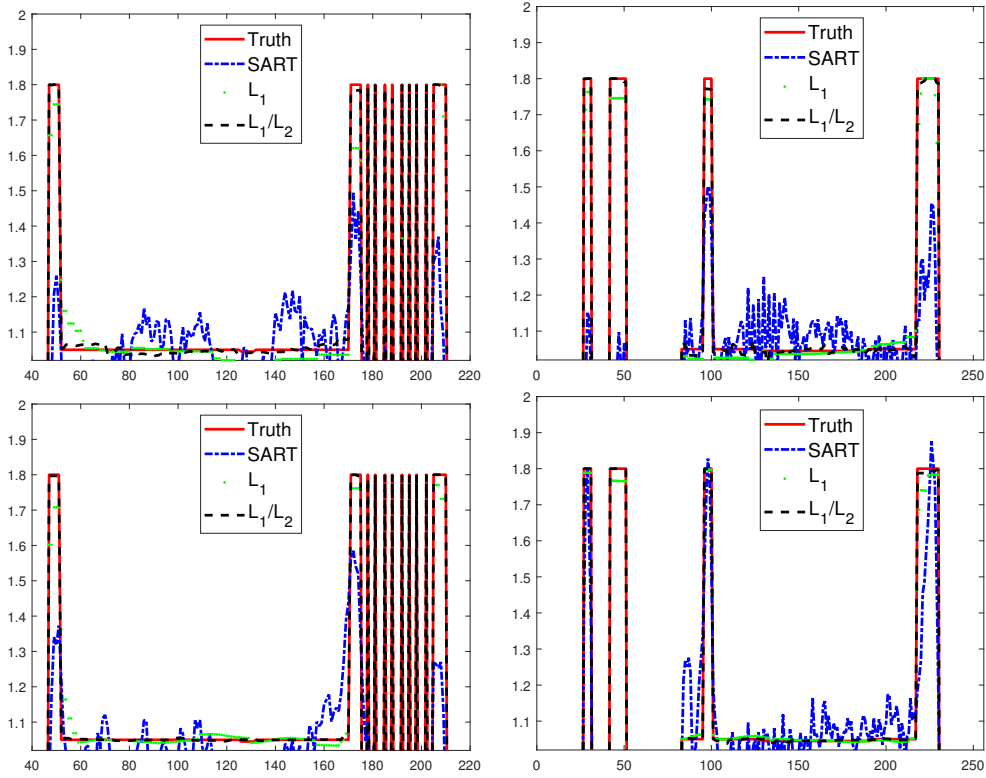


**Figure 10.** Noisy case: horizontal and vertical profiles generated via SART,  $L_1$ , and  $L_1/L_2$  in the range of projection  $90^\circ$  (top) and  $135^\circ$  (bottom) for the FB phantom.

- (a)  $\|\nabla f(x) - \nabla f(y)\|_2 \leq L\|x - y\|_2, \forall x, y;$
- (b)  $g(x) = \frac{L}{2}\|x\|_2^2 - f(x)$  is convex;
- (c)  $f(y) \leq f(x) + \langle \nabla f(x), y - x \rangle + \frac{L}{2}\|y - x\|_2^2, \forall x, y.$

We show in [Lemma A.3](#) that the gradient of the function  $f(\mathbf{x}) = \frac{1}{\|\mathbf{x}\|_2}$  is Lipschitz continuous on a set with a lower bound.

**Lemma A.3.** Given a function  $f(\mathbf{x}) = \frac{1}{\|\mathbf{x}\|_2}$  and a set  $\mathcal{M}_\epsilon := \{\mathbf{x} \mid \|\mathbf{x}\|_2 \geq \epsilon\}$  for a positive constant  $\epsilon > 0$ , we have

$$\|\nabla f(\mathbf{x}) - \nabla f(\mathbf{y})\|_2 \leq \frac{4}{\epsilon^3} \|\mathbf{x} - \mathbf{y}\|_2, \forall \mathbf{x}, \mathbf{y} \in \mathcal{M}_\epsilon.$$

*Proof.* Some calculations lead to

$$\begin{aligned}
& \|\nabla f(\mathbf{x}) - \nabla f(\mathbf{y})\|_2 = \left\| \frac{\mathbf{x}}{\|\mathbf{x}\|_2^3} - \frac{\mathbf{y}}{\|\mathbf{y}\|_2^3} \right\|_2 = \frac{1}{\|\mathbf{x}\|_2^3 \|\mathbf{y}\|_2^3} \left\| \|\mathbf{y}\|_2^3 \mathbf{x} - \|\mathbf{x}\|_2^3 \mathbf{y} \right\|_2 \\
& \leq \frac{1}{\|\mathbf{x}\|_2^2 \|\mathbf{y}\|_2^3} \left| \|\mathbf{y}\|_2^3 - \|\mathbf{x}\|_2^3 \right| + \frac{1}{\|\mathbf{y}\|_2^3} \|\mathbf{x} - \mathbf{y}\|_2 \\
& \leq \frac{1}{\|\mathbf{x}\|_2^2 \|\mathbf{y}\|_2^3} \left| \|\mathbf{y}\|_2 - \|\mathbf{x}\|_2 \right| \left( \|\mathbf{y}\|_2^2 + \|\mathbf{x}\|_2 \|\mathbf{y}\|_2 + \|\mathbf{x}\|_2^2 \right) + \frac{1}{\|\mathbf{y}\|_2^3} \|\mathbf{x} - \mathbf{y}\|_2 \\
& \leq \left( \frac{1}{\|\mathbf{x}\|_2^2 \|\mathbf{y}\|_2} + \frac{1}{\|\mathbf{x}\|_2 \|\mathbf{y}\|_2^2} + \frac{1}{\|\mathbf{y}\|_2^3} \right) \|\mathbf{y} - \mathbf{x}\|_2 + \frac{1}{\|\mathbf{y}\|_2^3} \|\mathbf{x} - \mathbf{y}\|_2 \leq \frac{4}{\epsilon^3} \|\mathbf{x} - \mathbf{y}\|_2.
\end{aligned}$$

### A.1. Proof of Lemma 4.2.

*Proof.* It follows from the optimality condition of the  $\mathbf{h}$ -subproblem in (4.1) that

$$(A.1) \quad -\frac{a^{(k+1)}}{\|\mathbf{h}^{(k+1)}\|_2^3} \mathbf{h}^{(k+1)} + \rho_2 \left( \mathbf{h}^{(k+1)} - \nabla u^{(k+1)} - \mathbf{b}_2^{(k)} \right) = 0,$$

where  $a^{(k)} := \|\nabla u^{(k)}\|_1$ . Using the dual update  $-\mathbf{b}_2^{(k+1)} = \mathbf{h}^{(k+1)} - \nabla u^{(k+1)} - \mathbf{b}_2^{(k)}$ , we have

$$(A.2) \quad \mathbf{b}_2^{(k+1)} = -\frac{a^{(k+1)}}{\rho_2} \frac{\mathbf{h}^{(k+1)}}{\|\mathbf{h}^{(k+1)}\|_2^3},$$

and similarly,

$$(A.3) \quad \mathbf{b}_2^{(k)} = -\frac{a^{(k)}}{\rho_2} \frac{\mathbf{h}^{(k)}}{\|\mathbf{h}^{(k)}\|_2^3}.$$

We can estimate

$$\begin{aligned}
& \|\mathbf{b}_2^{(k+1)} - \mathbf{b}_2^{(k)}\|_2 = \frac{1}{\rho_2} \left\| a^{(k+1)} \frac{\mathbf{h}^{(k+1)}}{\|\mathbf{h}^{(k+1)}\|_2^3} - a^{(k)} \frac{\mathbf{h}^{(k)}}{\|\mathbf{h}^{(k)}\|_2^3} \right\|_2 \\
(A.4) \quad & \leq \frac{1}{\rho_2} \left( \frac{1}{\|\mathbf{h}^{(k+1)}\|_2^2} |a^{(k+1)} - a^{(k)}| + a^{(k)} \left\| \frac{\mathbf{h}^{(k+1)}}{\|\mathbf{h}^{(k+1)}\|_2^3} - \frac{\mathbf{h}^{(k)}}{\|\mathbf{h}^{(k)}\|_2^3} \right\|_2 \right).
\end{aligned}$$

For the first term in (A.4), we use the facts that  $\|\mathbf{x}\|_1 \leq \sqrt{l} \|\mathbf{x}\|_2$  for a vector  $\mathbf{x}$  of the length of  $l$  and  $\|\nabla\|_2^2 \leq 8$ , thus leading to

$$\begin{aligned}
& |a^{(k+1)} - a^{(k)}| \leq \|\nabla(u^{(k+1)} - u^{(k)})\|_1 \leq \sqrt{2mn} \|\nabla(u^{(k+1)} - u^{(k)})\|_2 \\
(A.5) \quad & \leq \sqrt{2mn} \cdot \|\nabla\|_2 \cdot \|u^{(k+1)} - u^{(k)}\|_2 \leq 4\sqrt{mn} \|u^{(k+1)} - u^{(k)}\|_2.
\end{aligned}$$

Note that  $u \in \mathbb{R}^{m \times n}$  and  $\nabla u \in \mathbb{R}^{m \times n \times 2}$  (thus of length  $2mn$ .) Invoking Lemma A.3, we get

$$(A.6) \quad a^{(k)} \left\| \frac{\mathbf{h}^{(k+1)}}{\|\mathbf{h}^{(k+1)}\|_2^3} - \frac{\mathbf{h}^{(k)}}{\|\mathbf{h}^{(k)}\|_2^3} \right\|_2 \leq \frac{4M}{\epsilon^3} \|\mathbf{h}^{(k+1)} - \mathbf{h}^{(k)}\|_2.$$

By putting together (A.4)-(A.6) and using the Cauchy-Schwarz inequality, we get (4.2).  $\blacksquare$

**A.2. Proof of Lemma 4.3.** In order to prove Lemma 4.3, we show in Lemma A.4 that the augmented Lagrangian decreases sufficiently with respect to  $u^{(k)}$ . We need to discuss the constrained, unconstrained, and box constrained formulations separately.

**Lemma A.4.** *Under the same assumptions as in Lemma 4.3, we have*

$$(A.7) \quad \mathcal{L}(u^{(k+1)}, \mathbf{h}^{(k)}; \mathbf{b}_2^{(k)}) - \mathcal{L}(u^{(k)}, \mathbf{h}^{(k)}; \mathbf{b}_2^{(k)}) \leq -\frac{\bar{c}_1}{2} \|u^{(k+1)} - u^{(k)}\|_2^2,$$

holds for the augmented Lagrangian corresponding to  $L_1/L_2$ -con,  $L_1/L_2$ -uncon,  $L_1/L_2$ -con-box, or  $L_1/L_2$ -uncon-box. Here  $\bar{c}_1 > 0$  is a constant.

*Proof.* (1)  $L_1/L_2$ -con (the constrained case). Recall (3.1) for the  $u$ -subproblem in the constrained case that can be expressed as

$$u^{(k+1)} = \arg \min_u \frac{\|\nabla u\|_1}{h} + \frac{\rho_2}{2} \|\nabla u - \mathbf{h}^{(k)} + \mathbf{b}_2^{(k)}\|_2^2 \quad \text{s.t.} \quad Au = f,$$

with  $h = \|\mathbf{h}^{(k)}\|_2$ . The optimality conditions state that  $Au^{(k+1)} = f$  and there exists a vector  $w$  such that

$$(A.8) \quad 0 \in \frac{p^{(k+1)}}{h} + \rho_2 \nabla^T (\nabla u^{(k+1)} - \mathbf{h}^{(k)} + \mathbf{b}_2^{(k)}) + A^T w,$$

with  $p^{(k+1)} \in \partial \|\nabla u^{(k+1)}\|_1$ . By using the definition of subgradient and (A.8), we obtain that

$$(A.9) \quad \begin{aligned} & \mathcal{L}(u^{(k+1)}, \mathbf{h}^{(k)}; \mathbf{b}_2^{(k)}) - \mathcal{L}(u^{(k)}, \mathbf{h}^{(k)}; \mathbf{b}_2^{(k)}) \\ & \leq \left\langle \frac{p^{(k+1)}}{h}, u^{(k+1)} - u^{(k)} \right\rangle + \frac{\rho_2}{2} \|\nabla u^{(k+1)} - \mathbf{g}\|_2^2 - \frac{\rho_2}{2} \|\nabla u^{(k)} - \mathbf{g}\|_2^2 \\ & = -\langle w, Au^{(k+1)} - Au^{(k)} \rangle - \rho_2 \langle \nabla u^{(k+1)} - \mathbf{g}, \nabla u^{(k+1)} - \nabla u^{(k)} \rangle \\ & \quad + \frac{\rho_2}{2} \|\nabla u^{(k+1)} - \mathbf{g}\|_2^2 - \frac{\rho_2}{2} \|\nabla u^{(k)} - \mathbf{g}\|_2^2 \\ & = -\frac{\rho_2}{2} \|\nabla u^{(k+1)} - \nabla u^{(k)}\|_2^2, \end{aligned}$$

where we use  $Au^{(k+1)} = Au^{(k)} = f$ .

Denote  $\sigma$  as the smallest eigenvalue of the matrix  $A^T A + \nabla^T \nabla$ . We show  $\sigma$  is strictly positive. If  $\sigma = 0$ , there exists a vector  $x$  such that  $x^T (A^T A + \nabla^T \nabla) x = 0$ . It is straightforward that  $x^T A^T A x \geq 0$  and  $x^T \nabla^T \nabla x \geq 0$ . Therefore, one shall have  $x^T A^T A x = 0$  and  $x^T \nabla^T \nabla x = 0$ , which contradicts with Assumption A1 that  $\mathcal{N}(\nabla) \cap \mathcal{N}(A) = 0$ . Therefore, we have that

$$v^T (A^T A + \nabla^T \nabla) v \geq \sigma \|v\|_2^2, \quad \forall v.$$

By letting  $v = u^{(k+1)} - u^{(k)}$  and using  $Au^{(k+1)} = Au^{(k)} = f$ , we have

$$\|\nabla(u^{(k+1)} - u^{(k)})\|_2^2 \geq \sigma \|u^{(k+1)} - u^{(k)}\|_2^2.$$

Together with (A.9), we get

$$\mathcal{L}(u^{(k+1)}, \mathbf{h}^{(k)}; \mathbf{b}_2^{(k)}) - \mathcal{L}(u^{(k)}, \mathbf{h}^{(k)}; \mathbf{b}_2^{(k)}) \leq -\frac{\sigma \rho_2}{2} \|u^{(k+1)} - u^{(k)}\|_2^2.$$

(2)  $L_1/L_2$ -uncon (the unconstrained case). The function  $\mathcal{L}(u, \mathbf{h}^{(k)}; \mathbf{b}_2^{(k)})$  with fixed  $\mathbf{h}^{(k)}$  and  $\mathbf{b}_2^{(k)}$  is strongly convex with parameter  $\bar{c}_1\lambda$  (we can choose  $\rho_2 \geq \lambda$  as it is sufficiently large.) Then Lemma A.1 leads to

$$\mathcal{L}(u^{(k+1)}, \mathbf{h}^{(k)}; \mathbf{b}_2^{(k)}) \leq \mathcal{L}(u^{(k)}, \mathbf{h}^{(k)}; \mathbf{b}_2^{(k)}) - \frac{\sigma\lambda}{2} \|u^{(k+1)} - u^{(k)}\|_2^2.$$

(3)  $L_1/L_2$ -con-box (the constrained case with a box constraint). The proof is similar to the one in the  $L_1/L_2$ -con case, except for replacing the optimality condition (A.8) of the  $u$ -subproblem with

$$(A.10) \quad 0 \in \frac{p^{(k+1)}}{h} + \rho_2 \nabla^T (\nabla u^{(k+1)} - \mathbf{h}^{(k)} + \mathbf{b}_2^{(k)}) + A^T w_1 + w_2 - w_3,$$

where  $w_i, i = 1, 2, 3$  are the dual variables. Here, (A.9) still holds owing to the complementary slackness in the KKT conditions of (3.16), i.e.,

$$(u^{(k)} - c) \odot w_2 = (u^{(k+1)} - c) \odot w_2 = (d - u^{(k)}) \odot w_3 = (d - u^{(k+1)}) \odot w_3 = 0,$$

where  $\odot$  denotes pointwise multiplication.

(4)  $L_1/L_2$ -uncon-box (the unconstrained case with a box constraint). The optimality condition of (3.17) is

$$(A.11) \quad 0 \in \frac{p^{(k+1)}}{h} + \rho_2 \nabla^T (\nabla u^{(k+1)} - \mathbf{h}^{(k)} + \mathbf{b}_2^{(k)}) + A^T (Au^{(k+1)} - f) + w_2 - w_3,$$

Then we have

$$(A.12) \quad \begin{aligned} & \mathcal{L}(u^{(k+1)}, \mathbf{h}^{(k)}; \mathbf{b}_2^{(k)}) - \mathcal{L}(u^{(k)}, \mathbf{h}^{(k)}; \mathbf{b}_2^{(k)}) \\ & \leq \left\langle \frac{p^{(k+1)}}{h}, u^{(k+1)} - u^{(k)} \right\rangle + \frac{\rho_2}{2} \|\nabla u^{(k+1)} - \mathbf{g}\|_2^2 - \frac{\rho_2}{2} \|\nabla u^{(k)} - \mathbf{g}\|_2^2 \\ & \quad + \frac{\lambda}{2} \|Au^{(k+1)} - f\|_2^2 - \frac{\lambda}{2} \|Au^{(k)} - f\|_2^2 \\ & = - \left\langle Au^{(k+1)} - f, Au^{(k+1)} - Au^{(k)} \right\rangle - \rho_2 \langle \nabla u^{(k+1)} - \mathbf{g}, \nabla u^{(k+1)} - \nabla u^{(k)} \rangle \\ & \quad + \frac{\rho_2}{2} \|\nabla u^{(k+1)} - \mathbf{g}\|_2^2 - \frac{\rho_2}{2} \|\nabla u^{(k)} - \mathbf{g}\|_2^2 + \frac{\lambda}{2} \|Au^{(k+1)} - f\|_2^2 - \frac{\lambda}{2} \|Au^{(k)} - f\|_2^2 \\ & = - \frac{\rho_2}{2} \|\nabla u^{(k+1)} - \nabla u^{(k)}\|_2^2 - \frac{\lambda}{2} \|Au^{(k+1)} - Au^{(k)}\|_2^2, \end{aligned} \quad \blacksquare$$

By using  $\sigma$  as the smallest eigenvalue of  $\nabla^T \nabla + A^T A$ , we get

$$\mathcal{L}(u^{(k+1)}, \mathbf{h}^{(k)}; \mathbf{b}_2^{(k)}) \leq \mathcal{L}(u^{(k)}, \mathbf{h}^{(k)}; \mathbf{b}_2^{(k)}) - \frac{\sigma\lambda}{2} \|u^{(k+1)} - u^{(k)}\|_2^2.$$

In summary, we can choose  $\bar{c}_1$  to take either  $\sigma\rho_2$  for the constrained model or  $\sigma\lambda$  for the unconstrained one such that the inequality (A.7) holds.



Now we are ready to prove for [Lemma 4.3](#).

*Proof.* Denote  $a = \|u^{(k+1)}\|_1$  and  $L = \frac{4M}{\epsilon^3}$ . [Lemma 4.2](#) and [Lemma A.2](#) (c) lead to

$$(A.13) \quad \frac{a}{\|\mathbf{h}^{(k+1)}\|_2} \leq \frac{a}{\|\mathbf{h}^{(k)}\|_2} - \left\langle \frac{a\mathbf{h}^{(k)}}{\|\mathbf{h}^{(k)}\|_2^3}, \mathbf{h}^{(k+1)} - \mathbf{h}^{(k)} \right\rangle + \frac{L}{2} \|\mathbf{h}^{(k+1)} - \mathbf{h}^{(k)}\|_2^2.$$

Denoting  $\mathbf{z} = \nabla u^{(k+1)} + \mathbf{b}_2^{(k)}$  and using the optimality condition of  $\mathbf{h}^{(k+1)}$  ([A.1](#)), we get

$$(A.14) \quad \begin{aligned} & \frac{\rho_2}{2} \|\mathbf{h}^{(k+1)} - \mathbf{z}\|_2^2 - \frac{\rho_2}{2} \|\mathbf{h}^{(k)} - \mathbf{z}\|_2^2 \\ &= \frac{\rho_2}{2} \|\mathbf{h}^{(k+1)}\|_2^2 - \frac{\rho_2}{2} \|\mathbf{h}^{(k)}\|_2^2 - \left\langle -\frac{a\mathbf{h}^{(k+1)}}{\|\mathbf{h}^{(k+1)}\|_2^3} + \rho_2 \mathbf{h}^{(k+1)}, \mathbf{h}^{(k+1)} - \mathbf{h}^{(k)} \right\rangle \\ &= \left\langle \frac{a\mathbf{h}^{(k+1)}}{\|\mathbf{h}^{(k+1)}\|_2^3}, \mathbf{h}^{(k+1)} - \mathbf{h}^{(k)} \right\rangle - \frac{\rho_2}{2} \|\mathbf{h}^{(k+1)} - \mathbf{h}^{(k)}\|_2^2. \end{aligned}$$

Combining [\(A.13\)](#) and [\(A.14\)](#), we obtain

$$(A.15) \quad \begin{aligned} & \mathcal{L}(u^{(k+1)}, \mathbf{h}^{(k+1)}; \mathbf{b}_2^{(k)}) - \mathcal{L}(u^{(k+1)}, \mathbf{h}^{(k)}; \mathbf{b}_2^{(k)}) \\ & \leq \left\langle \frac{a\mathbf{h}^{(k+1)}}{\|\mathbf{h}^{(k+1)}\|_2^3} - \frac{a\mathbf{h}^{(k)}}{\|\mathbf{h}^{(k)}\|_2^3}, \mathbf{h}^{(k+1)} - \mathbf{h}^{(k)} \right\rangle - \frac{\rho_2 - L}{2} \|\mathbf{h}^{(k+1)} - \mathbf{h}^{(k)}\|_2^2 \\ & \leq \left\| \frac{a\mathbf{h}^{(k+1)}}{\|\mathbf{h}^{(k+1)}\|_2^3} - \frac{a\mathbf{h}^{(k)}}{\|\mathbf{h}^{(k)}\|_2^3} \right\|_2 \left\| \mathbf{h}^{(k+1)} - \mathbf{h}^{(k)} \right\|_2 - \frac{\rho_2 - L}{2} \left\| \mathbf{h}^{(k+1)} - \mathbf{h}^{(k)} \right\|_2^2 \\ & \leq -\frac{\rho_2 - 3L}{2} \|\mathbf{h}^{(k+1)} - \mathbf{h}^{(k)}\|_2^2. \end{aligned}$$

Lastly, from the update of  $\mathbf{b}_2$ , we compute

$$(A.16) \quad \begin{aligned} & \mathcal{L}(u^{(k+1)}, \mathbf{h}^{(k+1)}; \mathbf{b}_2^{(k+1)}) - \mathcal{L}(u^{(k+1)}, \mathbf{h}^{(k+1)}; \mathbf{b}_2^{(k)}) \\ &= \frac{\rho_2}{2} \left( \|\mathbf{b}_2^{(k)}\|_2^2 - \|\mathbf{b}_2^{(k+1)} - 2\mathbf{b}_2^{(k)}\|_2^2 \right) \leq \frac{\rho_2}{2} \|\mathbf{b}_2^{(k+1)} - \mathbf{b}_2^{(k)}\|_2^2. \end{aligned}$$

By putting the inequalities [\(A.7\)](#), [\(A.15\)](#), and [\(A.16\)](#) together with [Lemma 4.2](#), we have

$$\mathcal{L}(u^{(k+1)}, \mathbf{h}^{(k+1)}; \mathbf{b}_2^{(k+1)}) \leq \mathcal{L}(u^{(k)}, \mathbf{h}^{(k)}; \mathbf{b}_2^{(k)}) - c_1 \|u^{(k+1)} - u^{(k)}\|_2^2 - c_2 \|\mathbf{h}^{(k)} - \mathbf{h}^{(k+1)}\|_2^2,$$

where  $c_1 = \frac{\bar{c}_1}{2} - \frac{16mn}{\rho_2 \epsilon^4}$  and  $c_2 = \frac{\rho_2 \epsilon^3 - 12M}{2\epsilon^3} - \frac{16M^2}{\rho_2 \epsilon^6}$ . For sufficiently large  $\rho_2$ , we can have  $c_1, c_2 > 0$ . ■

*Remark A.5.* It seems that we need a very large value of  $\rho_2$  to guarantee  $c_1, c_2 > 0$  in [Lemma 4.3](#). Fortunately, it is just a sufficient condition for convergence and we can choose a reasonable value of  $\rho_2$  in practice.

### A.3. Proof of Lemma 4.4.

*Proof.* To accommodate all the models (constrained/unconstrained and with/without box), we express the optimality condition of (4.1) as follows,

$$(A.17) \quad \begin{cases} \frac{p^{(k+1)}}{\|\mathbf{h}^{(k)}\|_2} + q^{(k+1)} + r^{(k+1)} + \rho_2 \nabla^T (\nabla u^{(k+1)} - \mathbf{h}^{(k)} + \mathbf{b}_2^{(k)}) = 0 \\ -\frac{\|\nabla u^{(k+1)}\|_1}{\|\mathbf{h}^{(k+1)}\|_2^3} \mathbf{h}^{(k+1)} + \rho_2 (\mathbf{h}^{(k+1)} - \nabla u^{(k+1)} - \mathbf{b}_2^{(k)}) = 0 \\ \mathbf{b}_2^{(k+1)} = \mathbf{b}_2^{(k)} + \nabla u^{(k+1)} - \mathbf{h}^{(k+1)}, \end{cases}$$

where  $p^{(k+1)} \in \partial \|\nabla u^{(k+1)}\|_1$ ,  $q^{(k+1)}$  is either equal to  $\lambda A^T (Au^{(k+1)} - f)$  for the unconstrained problem or belongs to  $\partial(\Pi_{Au=f}(u^{(k+1)}))$  for the constrained case, and  $r^{(k+1)}$  either belongs to  $\partial(\Pi_{[c,d]}(u^{(k+1)}))$  with the box constraint or zero otherwise. Let  $\eta_1^{(k+1)}, \eta_2^{(k+1)}, \eta_3^{(k+1)}$  be

$$(A.18) \quad \begin{cases} \eta_1^{(k+1)} := \frac{p^{(k+1)}}{\|\mathbf{h}^{(k+1)}\|_2} + q^{(k+1)} + r^{(k+1)} + \rho_2 \nabla^T (\nabla u^{(k+1)} - \mathbf{h}^{(k+1)} + \mathbf{b}_2^{(k+1)}) \\ \eta_2^{(k+1)} := -\frac{\|\nabla u^{(k+1)}\|_1}{\|\mathbf{h}^{(k+1)}\|_2^3} \mathbf{h}^{(k+1)} + \rho_2 (\mathbf{h}^{(k+1)} - \nabla u^{(k+1)} - \mathbf{b}_2^{(k+1)}) \\ \eta_3^{(k+1)} := \rho_2 (\nabla u^{(k+1)} - \mathbf{h}^{(k+1)}). \end{cases}$$

Clearly, we have

$$\begin{aligned} \eta_1^{(k+1)} &\in \partial_u \mathcal{L}(u^{(k+1)}, \mathbf{h}^{(k+1)}, \mathbf{b}_2^{(k+1)}) \\ \eta_2^{(k+1)} &\in \partial_{\mathbf{h}} \mathcal{L}(u^{(k+1)}, \mathbf{h}^{(k+1)}, \mathbf{b}_2^{(k+1)}) \\ \eta_3^{(k+1)} &\in \partial_{\mathbf{b}_2} \mathcal{L}(u^{(k+1)}, \mathbf{h}^{(k+1)}, \mathbf{b}_2^{(k+1)}), \end{aligned}$$

for  $\mathcal{L} = \mathcal{L}_{\text{con}}, \mathcal{L}_{\text{uncon}}$ , or  $\mathcal{L}_{\text{box}}$ . Combining (A.17) and (A.18) leads to

$$\begin{cases} \eta_1^{(k+1)} = -\frac{p^{(k+1)}}{\|\mathbf{h}^{(k)}\|_2} + \frac{p^{(k+1)}}{\|\mathbf{h}^{(k+1)}\|_2} + \rho_2 \nabla^T (\mathbf{h}^{(k)} - \mathbf{h}^{(k+1)}) + \rho_2 \nabla^T (\mathbf{b}_2^{(k+1)} - \mathbf{b}_2^{(k)}) \\ \eta_2^{(k+1)} = \rho_2 (\mathbf{b}_2^{(k)} - \mathbf{b}_2^{(k+1)}) \\ \eta_3^{(k+1)} = \rho_2 (\mathbf{b}_2^{(k+1)} - \mathbf{b}_2^{(k)}). \end{cases}$$

The chain rule of subgradient [23] suggests that  $\partial \|\nabla u\|_1 = \nabla^T \mathbf{q}$ , where

$$\mathbf{q} = \{\mathbf{q} \mid \langle \mathbf{q}, \nabla u \rangle_Y = \|\nabla u\|_1, |q_{ijk}| \leq 1, \forall i, j, k\}.$$

Therefore, we have an upper bound for  $\|p^{(k+1)}\|_2 \leq \|\nabla^T\|_2 \|\mathbf{q}^{(k+1)}\|_2 \leq 2\sqrt{2mn}$ . Simple calculations show that

$$\begin{aligned} &\left\| \frac{p^{(k+1)}}{\|\mathbf{h}^{(k)}\|_2} - \frac{p^{(k+1)}}{\|\mathbf{h}^{(k+1)}\|_2} \right\|_2 = \left| \frac{1}{\|\mathbf{h}^{(k)}\|_2} - \frac{1}{\|\mathbf{h}^{(k+1)}\|_2} \right| \|p^{(k+1)}\|_2 \\ &\leq \frac{1}{\epsilon^2} \|\mathbf{h}^{(k+1)} - \mathbf{h}^{(k)}\|_2 \|p^{(k+1)}\|_2 \leq \frac{2\sqrt{2mn}}{\epsilon^2} \|\mathbf{h}^{(k+1)} - \mathbf{h}^{(k)}\|_2. \end{aligned}$$

Finally, by setting  $\gamma = \max\{26\rho^2, 24\rho^2 + \frac{24mn}{\epsilon^4}\}$ , (4.4) follows immediately. ■

## REFERENCES

- [1] K. A. AND M. SLANEY, *Principles of Computerized Tomographic Imaging*, SIAM, 2001.
- [2] A. H. ANDERSEN AND A. C. KAK, *Simultaneous algebraic reconstruction technique (SART): a superior implementation of the ART algorithm*, *Ultrason. Imaging*, 6 (1984), pp. 81–94.
- [3] C. AVINASH AND S. MALCOLM, *Principles of computerized tomographic imaging*, Society for Industrial and Applied Mathematics, Philadelphia, PA, USA, 2001.
- [4] D. BOUBLIL, M. ELAD, J. SHTOK, AND M. ZIBULEVSKY, *Spatially-adaptive reconstruction in computed tomography using neural networks*, *IEEE Trans. Med. Imaging*, 34 (2015), pp. 1474–1485.
- [5] S. BOYD, N. PARIKH, E. CHU, B. PELEATO, AND J. ECKSTEIN, *Distributed optimization and statistical learning via the alternating direction method of multipliers*, *Found. Trends Mach. Learn.*, 3 (2011), pp. 1–122.
- [6] J. T. BUSHBERG AND J. M. BOONE, *The essential physics of medical imaging*, Lippincott Williams & Wilkins, 2011.
- [7] E. J. CANDÉS, M. B. WAKIN, AND S. P. BOYD, *Enhancing sparsity by reweighted  $\ell_1$  minimization*, *J Fourier Anal Appl.*, 14 (2008), pp. 877–905.
- [8] A. CHAMBOLLE, *An algorithm for total variation minimization and applications*, *J Math Imaging Vis.*, 20 (2004), pp. 89–97.
- [9] A. CHAMBOLLE AND T. POCK, *A first-order primal-dual algorithm for convex problems with applications to imaging*, *J Math Imaging Vis.*, 40 (2011).
- [10] R. H. CHAN AND J. MA, *A multiplicative iterative algorithm for box-constrained penalized likelihood image restoration*, *IEEE Trans. Image Process.*, 21 (2012), pp. 3168–3181.
- [11] T. CHAN AND J. SHEN, *Image processing and analysis: variational, PDE, wavelet, and stochastic methods*, Siam, 2005.
- [12] R. CHARTRAND, *Exact reconstruction of sparse signals via nonconvex minimization*, *IEEE Signal Process. Lett.*, 10 (2007), pp. 707–710.
- [13] Z. CHEN, X. JIN, L. LI, AND G. WANG, *A limited-angle CT reconstruction method based on anisotropic TV minimization*, *Phys. Med. Biol.*, 58 (2013), p. 2119.
- [14] B. DE MAN AND J. A. FESSLER, *Statistical iterative reconstruction for x-ray computed tomography*, *Bio. Math.: Promising Dir. in Imaging, Therapy Plan., Inverse Prob.*, (2010), pp. 113–40.
- [15] I. A. ELBAKRI AND J. A. FESSLER, *Statistical image reconstruction for polyenergetic x-ray computed tomography*, *IEEE Trans. Med. Imaging*, 21 (2002), pp. 89–99.
- [16] L. A. FELDKAMP, L. C. DAVIS, AND J. W. KRESS, *Practical cone-beam algorithm*, *J. Opt. Soc. Am. A*, 1 (1984), pp. 612–619.
- [17] J. FRIKEL AND E. T. QUINTO, *Characterization and reduction of artifacts in limited angle tomography*, *Inverse Probl.*, 29 (2013), p. 125007.
- [18] H. GAO, L. ZHANG, Y. XING, Z. CHEN, J. ZHANG, AND J. CHENG, *Volumetric imaging from a multisegment straight-line trajectory and a practical reconstruction algorithm*, *Opt. Eng.*, 46 (2007), p. 077004.
- [19] S. GAZZOLA, P. C. HANSEN, AND J. G. NAGY, *IR tools: a MATLAB package of iterative regularization methods and large-scale test problems*, *Numer. Algorithms*, 81 (2019), pp. 773–811.
- [20] T. GOLDSTEIN AND S. OSHER, *The split Bregman method for  $L_1$ -regularized problems*, *SIAM J. Imaging Sci.*, 2 (2009), pp. 323–343.
- [21] K. GUO, D. HAN, AND T. WU, *Convergence of alternating direction method for minimizing sum of two nonconvex functions with linear constraints*, *Int. J. of Comput. Math.*, 94 (2017), pp. 1653–1669.
- [22] P. C. HANSEN AND M. SAXILD-HANSEN, *AIR tools — MATLAB package of algebraic iterative reconstruction methods*, *J. Comput. Appl. Math.*, 236 (2012), pp. 2167–2178.
- [23] J. B. HIRIART-URRUTY AND C. LEMARÉCHAL, *Convex Analysis and Minimization Algorithms*, Springer Verlag, Heidelberg, 1996. Two volumes - 2nd printing.
- [24] M. HONG, Z.-Q. LUO, AND M. RAZAVIYAYN, *Convergence analysis of alternating direction method of multipliers for a family of nonconvex problems*, *SIAM J. Optim.*, 26 (2016), pp. 337–364.
- [25] Y. HUANG, O. TAUBMANN, X. HUANG, V. HAASE, G. LAURITSCH, AND A. MAIER, *Scale-space anisotropic total variation for limited angle tomography*, *IEEE Trans. Radiat. Plasma Med. Sci.*, 2 (2018), pp. 307–314.
- [26] X. JIA, B. DONG, Y. LOU, AND S. B. JIANG, *GPU-based iterative cone-beam CT reconstruction using*

- tight frame regularization*, Phys. Med. Biol., 56 (2011), p. 3787.
- [27] X. JIA, Y. LOU, R. LI, W. Y. SONG, AND S. B. JIANG, *GPU-based fast cone beam CT reconstruction from undersampled and noisy projection data via total variation*, Med. Phys., 37 (2010), pp. 1757–1760.
- [28] M. JIANG AND G. WANG, *Convergence of the simultaneous algebraic reconstruction technique (SART)*, IEEE Trans. Image Process., 12 (2003), pp. 957–961.
- [29] X. JIN, L. LI, Z. CHEN, L. ZHANG, AND Y. XING, *Motion-compensated reconstruction method based on rigid motion model with multi-object*, Tsinghua Sci. Technol., 15 (2010), pp. 120–126.
- [30] K. KAN, S. WU FUNG, AND L. RUTHOTTO, *PNKH-B: A projected Newton-Krylov method for large-scale bound-constrained optimization*, arXiv preprint arXiv:2005.13639, (2020).
- [31] G. LI AND T. K. PONG, *Global convergence of splitting methods for nonconvex composite optimization*, SIAM J. Optim., 25 (2015), pp. 2434–2460.
- [32] F. LIU, J. ROSENBERGER, Y. LOU, R. HOSSEINI, J. SU, AND S. WANG, *Graph regularized EEG source imaging with in-class consistency and out-class discrimination*, IEEE Trans. Big Data, 3 (2017), pp. 378–391.
- [33] F. LIU, S. WANG, J. QIN, Y. LOU, AND J. ROSENBERGER, *Estimating latent brain sources with low-rank representation and graph regularization*, in Int. Conf. Brain Info., Springer, 2018, pp. 304–316.
- [34] Y. LOU AND M. YAN, *Fast  $L_1$ - $L_2$  minimization via a proximal operator*, J. Sci. Comput., 74 (2018), pp. 767–785.
- [35] Y. LOU, P. YIN, Q. HE, AND J. XIN, *Computing sparse representation in a highly coherent dictionary based on difference of  $L_1$  and  $L_2$* , J. Sci. Comput., 64 (2015), pp. 178–196.
- [36] Y. LOU, P. YIN, AND J. XIN, *Point source super-resolution via non-convex  $l_1$  based methods*, J. Sci. Comput., 68 (2016), pp. 1082–1100.
- [37] Y. LOU, T. ZENG, S. OSHER, AND J. XIN, *A weighted difference of anisotropic and isotropic total variation model for image processing*, SIAM J. Imaging Sci., 8 (2015), pp. 1798–1823.
- [38] Y. LOU, X. ZHANG, S. J. OSHER, AND A. L. BERTOZZI, *Image recovery via nonlocal operators*, J. Sci. Comput., 42 (2010), pp. 185–197.
- [39] X. LUO, W. YU, AND C. WANG, *An image reconstruction method based on total variation and wavelet tight frame for limited-angle CT*, IEEE Access, 6 (2017), pp. 1461–1470.
- [40] M. LUSTIG, D. L. DONOHO, AND J. M. PAULY, *Sparse MRI: The application of compressed sensing for rapid MR imaging*, Magnet. Reson. Med., 58 (2007), pp. 1182–1195.
- [41] D. LV, Q. ZHOU, J. K. CHOI, J. LI, AND X. ZHANG, *Nonlocal TV-Gaussian prior for Bayesian inverse problems with applications to limited CT reconstruction*, Inverse Probl. Imag., 14 (2020), p. 117.
- [42] J. LV AND Y. FAN, *A unified approach to model selection and sparse recovery using regularized least squares*, Ann. Appl. Stat., (2009), pp. 3498–3528.
- [43] T. MA, Y. LOU, AND T. HUANG, *Truncated  $l_1$ - $l_2$  models for sparse recovery and rank minimization*, SIAM J. Imaging Sci., 10 (2017), pp. 1346–1380.
- [44] L. V. NGUYEN, *How strong are streak artifacts in limited angle computed tomography?*, Inverse Probl., 31 (2015), p. 055003.
- [45] J. NOCEDAL AND S. J. WRIGHT, *Numerical Optimization*, Springer, 2006.
- [46] J.-S. PANG AND M. TAO, *Decomposition methods for computing directional stationary solutions of a class of nonsmooth nonconvex optimization problems*, SIAM J. Optim., 28 (2018), pp. 1640–1669.
- [47] E. T. QUINTO, *Exterior and limited-angle tomography in non-destructive evaluation*, Inverse Probl., 14 (1998), p. 339.
- [48] Y. RAHIMI, C. WANG, H. DONG, AND Y. LOU, *A scale invariant approach for sparse signal recovery*, SIAM J. Sci. Comput., 41 (2019), pp. A3649–A3672.
- [49] L. RUDIN, S. OSHER, AND E. FATEMI, *Nonlinear total variation based noise removal algorithms*, Physica D, 60 (1992), pp. 259–268.
- [50] L. A. SHEPP AND B. F. LOGAN, *The Fourier reconstruction of a head section*, IEEE Trans. Nucl. Sci., 21 (1974), pp. 21–43.
- [51] E. Y. SIDKY, C. KAO, AND X. PAN, *Accurate image reconstruction from few-views and limited-angle data in divergent-beam CT*, J. X-Ray Sci. Technol., 14 (2006), pp. 1–21.
- [52] E. Y. SIDKY AND X. PAN, *Image reconstruction in circular cone-beam computed tomography by constrained, total-variation minimization*, Phys. Med. Biol., 53 (2008), p. 4777.
- [53] X. TANG, J. HSIEH, R. A. NILSEN, S. DUTTA, D. SAMSONOV, AND A. HAGIWARA, *A three-dimensional-*

- weighted cone beam filtered backprojection (CB-FBP) algorithm for image reconstruction in volumetric CT-helical scanning*, Phys. Med. Biol., 51 (2006), p. 855.
- [54] R. TOVEY, M. BENNING, C. BRUNE, M. J. LAGERWERF, S. M. COLLINS, R. K. LEARY, P. A. MIDGLEY, AND C.-B. SCHÖNLIEB, *Directional sinogram inpainting for limited angle tomography*, Inverse Probl., 35 (2019), p. 024004.
- [55] C. WANG, R. CHAN, M. NIKOLOVA, R. PLEMMONS, AND S. PRASAD, *Nonconvex optimization for 3-dimensional point source localization using a rotating point spread function*, SIAM J. Imaging Sci., 12 (2019), pp. 259–286.
- [56] C. WANG, M. YAN, Y. RAHIMI, AND Y. LOU, *Accelerated schemes for the  $L_1/L_2$  minimization*, IEEE Trans. Signal Process., 68 (2020), pp. 2660–2669.
- [57] F. WANG, W. CAO, AND Z. XU, *Convergence of multi-block Bregman ADMM for nonconvex composite problems*, Sci. China Info. Sci., 61 (2018), pp. 122101:1–12.
- [58] G. WANG, Y. ZHANG, X. YE, AND X. MOU, *Machine Learning for Tomographic Imaging*, 2053-2563, IOP Publishing, 2019.
- [59] Y. WANG, W. YIN, AND J. ZENG, *Global convergence of ADMM in nonconvex nonsmooth optimization*, J. Sci. Comput., 78 (2019), pp. 29–63.
- [60] Z. WANG, A. C. BOVIK, H. R. SHEIKH, AND E. P. SIMONCELLI, *Image quality assessment: From error visibility to structural similarity*, IEEE Trans. Image Process., 13 (2004), pp. 600–612.
- [61] Z. WANG, Z. HUANG, Z. CHEN, L. ZHANG, X. JIANG, K. KANG, H. YIN, Z. WANG, AND M. STAMPANONI, *Low-dose multiple-information retrieval algorithm for x-ray grating-based imaging*, Nucl. Instrum. Methods Phys., 635 (2011), pp. 103–107.
- [62] Z. WEI, B. LIU, B. DONG, AND L. WEI, *A joint reconstruction and segmentation method for limited-angle x-ray tomography*, IEEE Access, 6 (2018), pp. 7780–7791.
- [63] Z. XU, X. CHANG, F. XU, AND H. ZHANG,  *$l_{1/2}$  regularization: A thresholding representation theory and a fast solver*, IEEE Trans. Neural Netw. Learn. Syst., 23 (2012), pp. 1013–1027.
- [64] P. YIN, E. ESSER, AND J. XIN, *Ratio and difference of  $l_1$  and  $l_2$  norms and sparse representation with coherent dictionaries*, Comm. Info. Systems, 14 (2014), pp. 87–109.
- [65] H. YU AND G. WANG, *A soft-threshold filtering approach for reconstruction from a limited number of projections*, Phys. Med. Biol., 55 (2010), p. 3905.
- [66] Z. YU, F. NOO, F. DENNERLEIN, A. WUNDERLICH, G. LAURITSCH, AND J. HORNEGGER, *Simulation tools for two-dimensional experiments in x-ray computed tomography using the FORBILD head phantom*, Phys. Med. Biol., 57 (2012), p. N237.
- [67] S. ZHANG AND J. XIN, *Minimization of transformed  $L_1$  penalty: Closed form representation and iterative thresholding algorithms*, Comm. Math. Sci., 15 (2017), pp. 511–537.
- [68] S. ZHANG AND J. XIN, *Minimization of transformed  $L_1$  penalty: Theory, difference of convex function algorithm, and robust application in compressed sensing*, Math. Program., 169 (2018), pp. 307–336.
- [69] Y. ZHANG, H.-P. CHAN, B. SAHINER, J. WEI, M. M. GOODSITT, L. M. HADJIISKI, J. GE, AND C. ZHOU, *A comparative study of limited-angle cone-beam reconstruction methods for breast tomosynthesis*, Med. Phys., 33 (2006), pp. 3781–3795.